Identification of reversible and irreversible deactivation of MDA catalysts: A key to design a viable process

Antoine Beuque, Valentin Valtchev, Svetlana Mintova, Jean-Pierre Gilson, Ludovic Pinard

Identification of reversible and irreversible deactivation of MDA catalysts: a key to design a viable process

Antoine Beuque[1,*], Valentin Valtchev[2], Svetlana Mintova[2], Jean-Pierre Gilson[2], Ludovic Pinard[2,*]

[1]Institut de Chimie des Milieux et Matériaux de Poitiers (ICM2P), UMR 7285 CNRS, 4 Rue Michel Brunet, Bâtiment B27, 86073 Poitiers Cedex 9–France

[2]Laboratoire Catalyse & Spectrochimie, CNRS, ENSICAEN, Normandy University-Caen 6, boulevard Maréchal Juin, 14050 Caen, FRANCE

*Corresponding authors: ludovic.pinard@ensicaen.fr,

antoine.beuque@univ-poitiers.fr

Abstract

We report a detailed kinetic study of methane dehydroaromatization on three bifunctional Mo/HZSM-5 catalysts (0.9 wt.%, 2.7 wt.%, and 17.2 wt. % Mo). Two main deactivation modes are present: (i) irreversible damage by zeolite amorphization during the isothermal pre-treatment in an inert atmosphere and (ii) reversible deactivation by coke deposition ("soft", "hard" and carbide species). The former occurs at high Mo loading (> 4.0 w%) and provides low activity catalysts. Catalysts with a lower and well-balanced molybdenum loading (< 4 w%) suffer mainly from the second deactivation mode. The catalyst decay is modelled by semi-empirical laws including time on stream and coke level. The latter initiates textural and structural catalyst modifications leading to an activity loss. Three deactivation descriptors, 1*:* coke level on the spent samples, *2:* loss of micropore volume, and *3:* monoclinic/orthorhombic phase transition of the zeolite are identified. Further characterization indicates that both molybdenum and carbon species are responsible for the catalytic deactivation of well-balanced catalysts. At least 50% of the initially dispersed molybdenum migrates to the external surface of the zeolite to form large clusters of molybdenum carbide. The coke extracted from the zeolite micropores are confirmed to be mainly unsubstituted polyaromatics.

Keywords: Zeolite, Methane dehydroaromatization, Pre-treatment, Deactivation, Dealumination, Coke, Modelling, Descriptors, Carbide migration

Graphical abstract

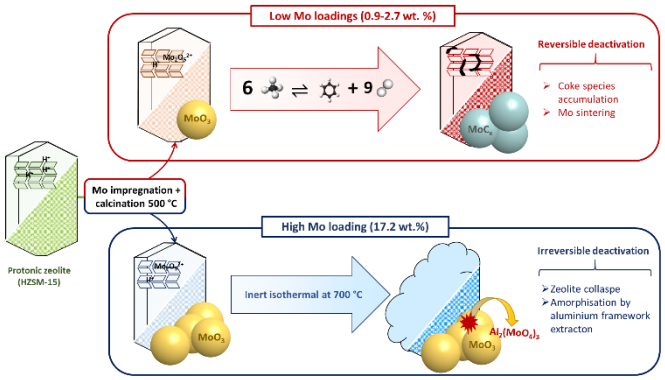

Introduction

Amongst the current worldwide energy challenges, greenhouse gas emission reduction and a forecasted increase of petrochemicals to fuels ratio are shifting the energy landscape to cleaner alternative sources. Natural- and bio-gas, an abundant, versatile and low-carbon, feedstock appears as an interesting feedstock for a cleaner chemical industry.[1,2] Methane, the most abundant compound in natural- and bio-gas, is currently used mainly in power plants for electricity generation. Its high chemical stability (first dissociation energy of C-H is 439 kJ mol^{-1})[3] is a challenge in its transformation to higher-value chemicals.[4,5]

Methane dehydroaromatization (MDA: 6 $CH_4 \leftrightharpoons C_6H_6 + 9\ H_2$), under non-oxidative conditions, over Mo/HZSM-5 bifunctional catalysts is one option to transform methane in H_2, a CO_2-free energy vector along with key building-blocks for petrochemistry.[6] Equilibrium thermodynamic conversion to benzene (~ 12.5 % at 700 °C) and rapid catalyst deactivation by coking at such high temperatures hinder its potential industrialization.[7,8]

Molybdenum containing MDA catalysts, where Mo is impregnated on a protonic HZSM-5 zeolite, are known to evolve continuously from pre-treatment to terminal deactivation. During calcination, Mo precursors migrate to Brønsted acid sites of the zeolite.[9] Their subsequent reduction to carbides produces active sites responsible for the production of aromatics, hydrogen and coke deposition on the catalyst. The latter is principally responsible for catalyst deactivation.[10]

The highly endothermic MDA reaction requires operating conditions outside the current comfort zone of zeolite based catalytic processes, involves complex mechanisms, and *operando* characterization highly difficult. These features render monitoring catalytic performances evolution arduous; the behaviour of such catalysts is therefore not yet fully understood.[11,12]

The nearly impossible use of *operando* characterization imposes to rely on more classical kinetic studies. Song et al. stated that ethylene is the main coke precursor leading to three

types of carbonaceous deposition throughout the catalyst lifetime: (i) molybdenum carbide, ii) graphitic carbon deposited as a layer near the molybdenum site (“soft” coke), and iii) polyaromatic compounds on acid sites (“hard” coke). The distinction between “soft” and “hard” coke species is defined by their oxidation temperature measured by thermogravimetry.[13,14]

Molybdenum active sites are believed to migrate from the Brønsted acid sites and sinter on the zeolite external surface, forming large Mo_2C clusters.[15–17] This migration favors “soft” coke deposition, assumed to be graphitic species near Mo sites or at the external surface; their exact role on catalytic performances has not yet been fully established. Hard coke grows progressively inside the zeolite micropores by poly-condensation, leading to catalyst deactivation by pore blocking. However, very recently, Hensen et al. emphasized that these two coke species have a similar chemical nature questioning their real impact in the reaction.[15,18,19] Indeed, part of these carbonaceous deposits could act like an organo-catalytic complex forming a hydrocarbon pool to produce aromatics.[20] The disagreements on a deactivation mechanism results from an absence of suitable spectroscopic analyses preventing a detailed composition of the coke.[21]

A remedy is the now well-established coke extraction, by a selective dissolution of the zeolite component of the spent catalysts, to determine the chemical composition of the coke trapped in the zeolite micropores.[22]

We showed previously that Mo species anchor on bridged Al pairs during the calcination, which is limiting the possible Mo exchange. The maximum amount of Mo anchored as $Mo_2O_5^{2+}$ inside the zeolite micropores amounts to 1.4 wt. % on a HZSM-5 with a Si/Al=15. While the remaining molybdenum is present on the external surface of the zeolite crystals as MoO_3.[23] The optimum level of molybdenum appears to be ~ 3 wt. %; at lower or higher Mo content, the catalysts display poor catalytic performances. In any case, all catalysts deactivate and coke deposition occurs with time on stream. At higher Mo content, partial

zeolite amorphization occurs. As this does not occur at lower Mo loading, the Mo/Al should influence the deactivation modes.

Based on the above, a more detailed study of the influence of the Mo/Al on the irreversible and reversible deactivations warrants further investigation. Moreover, since the catalyst is calcined at a lower temperature (500 °C) than the reaction (700 °C), the influence of the pre-treatment should be included in a kinetic study. We will therefore evaluate the catalyst from the pre-treatment stage to complete deactivation using three Mo/H-ZSM-5 catalysts differing only by their Mo loading: (i) very low Mo, 0.9 wt. % (0.9-MoHZ-15), (ii) optimal Mo, 2.7 wt. % (2.7-MoHZ-15), and (iii) high Mo, 17.2 wt. % (17.2-MoHZ-15).

The importance of fine-tuning the pre-treatment is first investigated on the high Mo containing catalyst (17.2-MoHZ-15) as irreversible zeolite amorphization occurs. On the two other catalysts, not drastically impacted by the inert thermal pre-treatment, three descriptors are used to evaluate their deactivation: coke content, residual microporous volume, and monoclinic/orthorhombic phase transition. Other parameters including coke amount, localization and chemical nature also contribute to the coking. As outlined in previous works, selective HF digestion of the inorganic fraction of the spent catalysts leaving intact the organic fractions is key to such a study; it brings molecular insights on the hydrocarbons trapped in a zeolite after reaction. Coking is typically a shape-selective process, progressively deactivating the catalyst.[23] In the present case, as at least 50% of the initially well-dispersed molybdenum migrates to the external zeolite surface as molybdenum carbides after 20 h of reaction, it is possible to shed a light on their nature.

2-Experimental

2.1. Catalyst preparation: The NH_4-ZSM-5 zeolite (CBV 3024E, Si/Al = 15, Zeolyst International) was first converted in protonic form (H-ZSM-5) by calcination under static air at 550 °C for 6 h with a heating rate of 2 °C min^{-1}. HZSM-5 supported Mo catalysts were

prepared by incipient wetness impregnation with an aqueous solution of ammonium heptamolybdate tetrahydrate (AHM, $(NH_4)_6Mo_7O_{24}.4H_2O$, Sigma Aldrich) with a concentration ranging from 0.0015 M to 0.030 M, equivalent to a Mo loading between 1 wt.% and 20 wt.%. 50 mL per gram of protonic zeolite. The solutions were added dropwise to the zeolite under magnetic stirring (400 rpm) at room temperature and equilibrated for 24 h. The catalyst was then dried under static air at 80 °C for 12 h and calcined at 500 °C with a heating rate of 2 °C min^{-1} for 6 h.

The resulting catalysts are denoted as X-MoHZ-15, where X represents the Mo loading (X = 0.9; 2.7 or 17.2).

2.2. Characterization of fresh catalysts: The molybdenum content of X-MoHZ-15 was determined by Inductively Coupled Plasma-Optical Emission Spectroscopy (ICP-OES) on an Optima 2000 DV (Perkin-Elmer). All samples are first dissolved in mixed acids (4 mL HNO_3 (68 %), 2 mL HCl (34-37 %), 2 mL HF (47-51 %), 42 mL H_2O and mineralized in an Anton-Paar Multiwave pro microwave reactor. The error tolerance calculated from 2 measurements of the same sample is +/- 0.1 wt.%.

Powder X-ray diffractograms were collected on a PANalytical Empyrean X-ray diffractometer with a Cu Kα radiation ($\lambda = 0.15418$ nm), in the 2θ 5 - 50° range with a scan speed of 0.033° s^{-1}. The morphology, homogeneity, and particle size were determined using a Scanning Electron Microscope (SEM, Philips XL30 FEG).

Nitrogen physisorption on the zeolite before and after Mo impregnation was measured at –196 °C on a Micromeritics 3Flex analyzer. Samples were outgassed at room temperature under vacuum for 15 h before each measurement. The micropore volume (V_{micro}) was calculated from the t-plot curve using the Harkins-Jura method and a thickness range between 4.5 and 5.5 Å. The mesopore volume (V_{meso}) was deduced by subtracting micropore volume from the total pore volume at $P/P_0 = 0.95$.

The nature and concentration of the zeolite acid sites before and after Mo impregnation were measured by pyridine adsorption monitored by infrared spectroscopy (FTIR) with a Nicolet 5700 apparatus with resolution 2 cm^{-1}.[24]

Raman spectra of fresh catalysts were recorded using a 532 nm laser focused on the sample equipped with a 100X microscope objective (NA=0.9, Olympus) with a power of 0.20 mW. The scattered light was guided through a 200 µm confocal hole analyzed by means of a 1800 grooves grating and Peltier-cooled CCD (ANDOR) as implemented in the Labram HR 800 spectrometer (HORIBA).

2.3. Catalytic evaluation: Methane dehydroaromatization was performed at atmospheric pressure in a fixed-bed quartz reactor (6 mm inner diameter) at 700 °C continuously fed with a (15/85) (v/v) N_2/CH_4 mixture (Air Liquide, purity: 99.999) at a flow rate of 0.84 L h^{-1} (STP). The gas hourly space velocity per gram of catalyst (GHSV) was 1.4 L h^{-1} g_{cat}^{-1} as reported elsewhere.[25] Before testing, catalysts were compacted under 3 tons, crushed and sieved (0.2-0.4 mm), and 0.6 g of the sieved catalyst loaded in the reactor. All samples were pre-treated at 700 °C under a nitrogen flow (3 L h^{-1}) for 1 h with a heating rate of 10 °C min^{-1}.

Gaseous effluents including hydrogen were analyzed online on a Varian CP-3800 gas chromatograph fitted with an FID detector connected to a fused silica J&W GS-Gaspro capillary column (60 m x 0.32 mm x 4 µm), and a TCD connected to a J&W PoraPLOT Q-HT capillary column (25 m x 0.53 mm x 20 µm). As analysis time is 30 min, no data were collected during the early stages of activation and induction. An HPR 20 QIC R&D mass spectrometer (Hiden Analytical) was connected to the effluent to monitor as a function of time-on-stream the mass-to-charge ratios 16, 27, 78, 92, and 128, corresponding to CH_4, $C_2H_3^+$, C_6H_6, C_7H_8, and $C_{10}H_8$, respectively.

The reaction was carried in a time on stream (ToS) from 5 min up to 20 hours. The feed gas was replaced at different ToS with nitrogen to desorb the most volatile products retained on the catalyst. The reactor was then rapidly cooled to 150 °C with a dry airflow to analyze the

retained hydrocarbons at 5 min, 10 min, 30 min, 1 h, 4 h, 10 h, or 20 h ToS. The recovered materials were referred to as $(X\text{-MoHZ-15})_Y$ where X stands for wt % Mo and Y for ToS.

2.4. Coke characterization: the coke content was measured using a SDT Q600 (TA instruments) thermal analyzer. After loading, each sample was first kept under a dry air flow of 100 mL min^{-1} for 30 min, then heated at 20 °C min^{-1} to 900 °C and held at this final temperature for 10 min. The combustion products, H_2O (m/z = 18), CO (m/z = 28), and CO_2 (m/z = 44) were continuously monitored by mass spectra (QG Hiden Analytical).

The chemical composition of coke was determined using the well-established procedure developed by Magnoux et al.[26] 300 mg of each coked samples were mineralized with 3 mL of a 51% hydrofluoric acid (HF) solution at room temperature for 30 min. The acid solution was then diluted with 18 mL of a boric acid solution ($[H_3BO_3]$ = 40 g L^{-1}) and neutralized (pH ~ 7) with 18 mL of a sodium bicarbonate solution ($[NaHCO_3]$ = 20 g L^{-1}). CH_2Cl_2 was then added to extract the hydrocarbons trapped in the zeolite. This fraction was referred to as "soluble coke" and the hydrocarbons recovered by filtration as "insoluble coke". The molecules of the soluble fraction were identified by GC-MS (Thermo Electron DSQ with a DB5 ms column).

Results and discussion

1. Evolution of catalysts under isothermal anaerobic pre-treatment

Three catalysts with different Mo loading are first calcined under air at 500 °C, then heated under a nitrogen flow for 1 hour at 700 °C. As the reaction takes place at 700 °C, only a partial catalyst picture is drawn when the characterization takes place after calcination at 500 °C.

Table 1 compares the different textural properties of catalysts before and after the inert pre-treatment.

Table 1: Characterization of the supported oxo-molybdate catalysts after calcination (500°C) and nitrogen activation (700 °C).

Catalyst	Fresh activated at 500°C				Nitrogen pre-treatment at 700 °C			
	Mo content [a] (wt. %)	Si/Al [a]	V_{micro} [b] ($cm^3\ g_{cat}^{-1}$)	[H+] [c] (µmol g_{cat}^{-1})	Mo content [a] (wt. %)	Si/Al [a]	V_{micro} [b] ($cm^3\ g_{cat}^{-1}$)	[H+] [c] (µmol g_{cat}^{-1})
HZ-15	0	15	0.13	500	0	15	0.13	350
0.9-MoHZ-15	0.9	15.1	0.13	380	0.9	15.4	0.13	340
2.7-MoHZ-15	2.7	15.2	0.12	338	2.4	15.5	0.12	290
17.2-MoHZ-15	17.2	14.4	0.09	264	13.6	14.5	0.01	0

[a] Mo content measured by ICP analysis.
[b] Micropore volume (V_{micro}) calculated from the t-plot curve using the Harkins-Jura method and a Thickness range between 4.5 and 5.5 Å.
[c] The Brønsted acid site concentration determined after pyridine desorption at 150 °C.

On the protonic zeolite, the IR spectra in the OH region before and after pre-treatment, **Figure S1,** shows a decrease of the BAS (Brønsted Acid Site) and EFAl (Extra-Framework Al) band intensities indicating zeolite dealumination and EFAL dehydroxylation at 700 °C. A loss of 150 µmol g_{cat}^{-1} (~ 30% of the initial BAS) is calculated, corresponding to the maximum ion-exchange capacity of molybdenum on the same zeolite. Upon molybdenum impregnation, this loss is mitigated for low Mo content (< 3 wt. %). In our previous study, [24] we shown that this loss of BAS is in good agreement with the theoretically determined values for the proportion of stabilized oxo-binuclear cation, which suggests oxo-molybdate moieties are anchored on paired aluminum protecting them from dealumination.

At low Mo loadings (< 2.7 wt. %), the ICP results indicate no significant Mo loss by sublimation during the inert atmosphere treatment; the molar Si/Al ratio and micropore volume are unchanged (**Table 1**).

Textural modifications appear at higher Mo loading: sample 17.2-MoHZ-15 loses 4 wt. % of its Mo after nitrogen pre-treatment and the decrease of the micropore volume indicates an amorphization of the zeolite which is further confirmed by XRD (**Figure 1.a**).

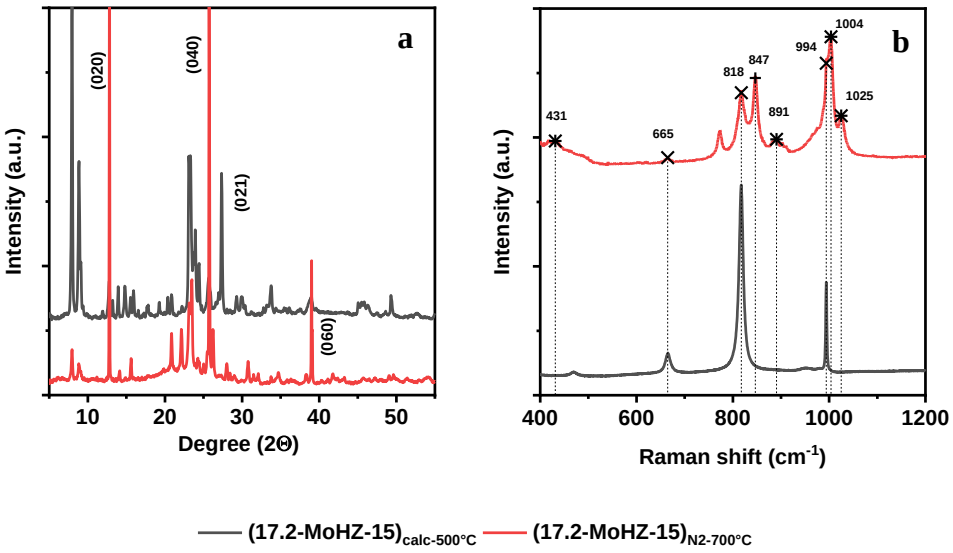

Figure 1: (a) XRD patterns and (b) Raman spectra of catalysts (17.2-MoHZ-15)$_{calc\text{-}500°C}$ and (17.2-MoHZ-15)$_{N2\text{-}700\ °C}$. ×, +, ✳ symbols represent MoO_3, MoO_2 and $Al_2(MoO_4)_3$, respectively.

The absence of the characteristic [0 2 1] peak of α-MoO_3 at 27.3° (JCPDS File No. 04–012-8070), observed on the 500°C calcined catalyst, and the intensity increase of the [0 k 0] α-MoO_3 peaks indicates possible morphological change. The initial α-MoO_3 crystals evolve with a preferred orientation and generate a lamellar structure during the inert pre-treatment as previously reported.[27] This is confirmed by SEM characterization of sample 17.2-MoHZ-15 (**Figure S2**). After calcination at 500 °C, numerous MoO_3 particles (~ 1 µm) are located on the external surface of zeolite crystals (**Figure S2.a**). After the inert pre-treatment at 700°C, the MoO_3 particle size is smaller (~ 0.1 µm) and homogeneously dispersed on the zeolite

external surface. A similar observation under reductive pre-treatment, albeit at lower temperatures (550-650°C) was reported.[28]

The presence of α-MoO_3 on the zeolite external surface are detected by Raman spectroscopy (**Figure 1.b)**; the intense and sharp bands at 666, 818, and 994 cm^{-1} indicative of an excess of Mo are present in the spectra.[29] After the inert pre-treatment at 700°C, a peak splitting at 847cm^{-1} and new bands at 431, 891, 1004, and 1025 cm^{-1} are emerged, indicating the presence of β-MoO_3 and $Al_2(MoO_4)_3$, respectively.[30,31] These bands are not observed for the two others catalysts (**Figure S3),** suggesting no significant formation of extra-framework species.

In a previous paper[24] we proposed that water released during activation is responsible for the zeolite collapse. These ~~new~~ results indicates that zeolite amorphization already takes place during the thermal treatment in the inert atmosphere. The large initial MoO_3 particles are thermally broken to form smaller MoO_3 crystals homogenously dispersed on the zeolite external surface where they may react with framework aluminum, progressively destroying first the outer surface and followed by the bulk leading to total zeolite amorphization.

Under oxidative treatment, the zeolite dealumination was attributed to the presence of Mo in the micropores after MoO_3 sublimation; this Mo in turn reacting with extra-framework Al to form a highly stable $Al_2(MoO_4)_3$ phase.[32]. This phenomenon has been already understood in detail [[32],[33], [34], [35]]. We show here that such a reaction takes already place during an inert pre-treatment at 700°C ultimately leading to the zeolite amorphization.

We therefore propose two pathways for zeolite amorphization: internal collapse or mediated by the external surface.

$$\xrightarrow[N_2\ 700\ °C]{MoO_3} Al_2(MoO_4)_3 + SiO_2 \qquad \text{(Eq.1)}$$

Hensen et al. also suggested zeolite amorphization from the interaction of oxo-molybdate anchored species with gas phase MoO_3 diffusing in the zeolite after sublimation as presented in Eq. 1.[32] On the other hand, Iglesia et al. proposed that the bulk MoO_3 species on the external zeolite surface extract AlO_X species from the framework (Si/Al molar ratio of 14.3) leading to a progressive trimming of the outer surface.[34] Such an amorphization also occurs in zeolites with lower Si/Al ratios (40 and 75), when no Mo moieties are anchored on the paired aluminum.[24]

The collapse of the zeolite crystals is further confirmed by TEM. **Figure 2** highlights also that the zeolite external surface of calcined 17.2-MoHZ-15 catalysts are damaged after pre-treatment at 700 °C under N_2. The presence of heterogeneous spots inside the zeolite crystals (red circles **Figure 2)** $(17.2\text{-MoHZ-15})_{N2\text{-}700°C}$ also indicates the structural collapse.

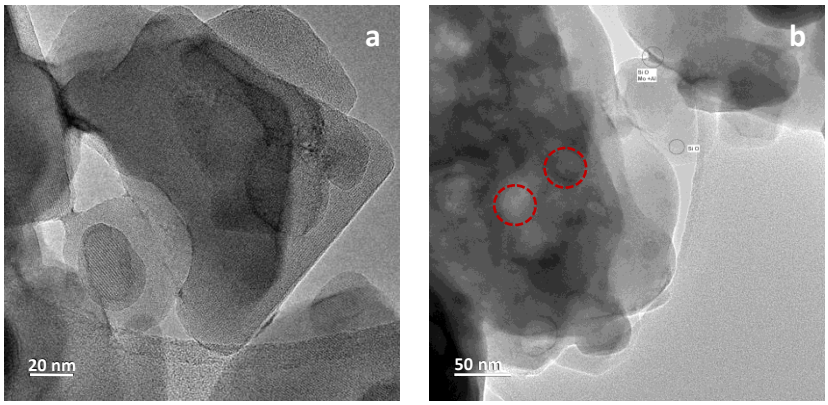

Figure 2: TEM pictures of (a) 17.2-MoHZ-15 and (b) $(17.2\text{-MoHZ-15})_{N2\text{-}700°C}$ catalysts. The red circles show the presence of lighter spot inside the zeolite crystal.

In summary, the catalyst with high Mo loading (17.2-MoHZ-15) is very sensitive to the pre-treatment conditions and already undergoes drastic degradations even under inert activation at 700 °C (**Figure 1**):

(i) Mo loss by sublimation after incipient wetness impregnation on the H-ZSM-5 is observed. The higher the Mo content, the more MoO_3 locates on the external surface thus facilitating its sublimation.

(ii) Morphologic transformation of a thermally stable orthorhombic α-MoO_3 to a metastable monoclinic phase β-MoO_3 is observed.

(iii) Collapse of the zeolite structure due to the formation of stable extra-framework species $Al_2(MoO_4)_3$ is occurred.

It is noteworthy that only the reduction treatment can protect the zeolite structure from high-temperature reaction with aggressive MoO_3 [28, 36, 37]

2. Evaluation of catalysts in methane dehydroaromatization reaction

The three catalysts are evaluated in methane dehydroaromatization at different time on stream (ToS: 5 min, 10 min, 30 min, 1 h, 4 h, 10 h, and 20 h) under identical operating conditions (700 °C, atmospheric pressure, and GHSV= 1.4 $L\,h^{-1}\,g_{cat}^{-1}$). The catalytic performances, *i.e.*, CH_4 conversion *vs.* ToS and cumulative yields after 20 hr are presented in **Figure 3b** and the catalysts deactivation is depicted in **Figure 3.a**. A maximum deviation of the results based on 7 tests of 10% indicates the good experimental reproducibility. The low catalytic activity of 17.2-MoHZ-15 is due to the zeolite amorphization as described above. The Benzene is always the major product, followed by heavier aromatics (mainly coke and naphthalene) as shown in **Figure 3.b**. Toluene and ethylene are present in smaller proportions. The Benzene selectivity for the optimized catalyst (i.e. 2.7-MoHZ-15) is ~ 65%, typical for the MDA reaction.[6] Methane conversion after 20 hours ToS is also in a good agreement with previous reports.[32]

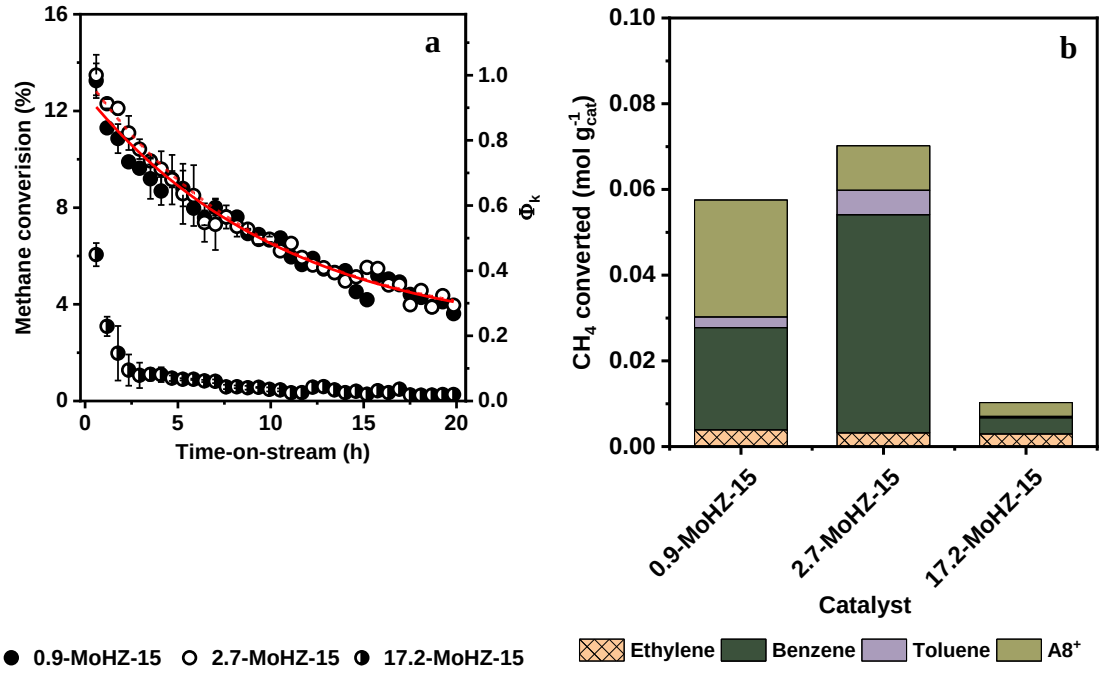

Figure 3: (a) Methane conversion and deactivation function ($\Phi_{k,}$ see part 4) *vs.* ToS (T=700°C, GHSV= 1.4 L h^{-1} g_{cat}^{-1}) and (b) cumulative product yields after 20 hours ToS. Full and dashed lines correspond to 0.9-MoHZ-15 and 2.7-MoHZ-15 fitting, respectively.

All MDA catalysts display the typical ToS behavior of Mo/HZSM-5 with three well-known steps[18,21]: (1) activation where no benzene is formed, (2) induction when aromatics yield increase, and (3) deactivation with a decrease in benzene yield (**Figure S5**). The activation time, related to the Mo loading[10] is 2 min, 10 min and 25 min on 0.9-MoHZ-15, 2.7-MoHZ-15 and 17.2-MoHZ-15, respectively, while the induction periods is 1 hour. The reaction is stopped at different ToS selected to study the catalyst evolution during these specific periods, while deactivation takes place. The coke levels at different ToS on each catalyst along with other characteristics are summarized in **Table 2**.

3. Deactivation mechanism on the 17.2 w% Mo catalyst

Since the 17.2-MoHZ-15 catalyst is already partially damaged after the pre-treatment at 700°C, its performance is poor. TEM pictures of the spent catalyst, 17.2-MoHZ-15_{20h}, after 20 h ToS **(Figure S4)** show large molybdenum carbide on the zeolite external surface surrounded by a carbon layer, as already observed elsewhere.[15]

The coke extracted after zeolite dissolution is totally insoluble in dichloromethane. Moreover, the amount of this insoluble coke is larger than the level of coke determined by the TG analysis (**Table 2**). The apparent discrepancy is explained by the ICP results indicating that this coke contains more than 60 wt. % of molybdenum. A large amount of molybdenum deposited on the external surface of zeolite crystals is therefore accounted too.

Table 2: Characterization of spent Mo/H-ZSM-5 catalysts recovered at different time on stream.

Sample	Mo[a] (wt. %)	Carbidic coke[b] (wt. %)	"Soft" coke[b] (wt. %)	"Hard" coke[b] (wt. %)	Micropore volume[c] ($cm^3\ g_{cat}^{-1}$)	Mesopore volume[d] ($cm^3\ g_{cat}^{-1}$)	Soluble coke (wt. %)	Insoluble coke	
								(wt. %)	H/C
0.9 wt. % Mo loading									
0.9-MoHZ-15	0.9	/	/	/	0.13	0.06	/	/	/
$(0.9\text{-MoHZ-15})_{N2\text{-}700°C}$	0.9	/	/	/	0.13	0.06	/	/	/
$(0.9\text{-MoHZ-15})_{2\ min}$	/	/	0.3	/	0.12	0.06	0.3	/	/
$(0.9\text{-MoHZ-15})_{5\ min}$	0.9	/	0.6	/	0.13	0.06	0.6	/	/
$(0.9\text{-MoHZ-15})_{10\ min}$	0.9	/	0.7	0.1	0.13	0.05	0.7	/	/
$(0.9\text{-MoHZ-15})_{30\ min}$	0.9	/	1.1	0.3	0.13	0.05	1.4	/	/
$(0.9\text{-MoHZ-15})_{1\ h}$	1.0	/	1.1	0.9	0.12	0.06	2.0	/	/
$(0.9\text{-MoHZ-15})_{4\ h}$	0.9	/	2.9	2.5	0.10	0.06	2.9	2.5	/
$(0.9\text{-MoHZ-15})_{10\ h}$	0.8	0.04	4.4	5.2	0.08	0.05	6.1	3.4	0.31
$(0.9\text{-MoHZ-15})_{20\ h}$	/	0.09	4.5	8.9	0.05	0.04	5.1	8.3	0.27
2.7 wt. % Mo loading									
2.7-MoHZ-15	2.7	/	/	/	0.12	0.06	/	/	/
$(2.7\text{-MoHZ-15})_{N2\text{-}700}$	2.4	/	/	/	0.12	0.06	/	/	/
$(2.7\text{-MoHZ-15})_{2\ min}$	/	/	/	/	/	/	/	/	/
$(2.7\text{-MoHZ-15})_{5\ min}$	2.4	/	/	/	/	/	/	/	/
$(2.7\text{-MoHZ-15})_{10\ min}$	2.3	/	0.8	0.7	0.12	0.06	1.5	/	/
$(2.7\text{-MoHZ-15})_{1\ h}$	2.2	/	1.5	0.8	0.11	0.06	2.3	/	0.41
$(2.7\text{-MoHZ-15})_{4\ h}$	2.3	0.02	3.2	1.9	0.10	0.06	2.9	2.2	0.43
$(2.7\text{-MoHZ-15})_{10\ h}$	2.4	0.14	4.2	3.9	0.09	0.05	1.7	6.4	/
$(2.7\text{-MoHZ-15})_{20\ h}$	/	0.18	6.1	6.2	0.06	0.04	1.3	11.0	0.32
17.2 wt. % Mo loading									
17.2-MoHZ-15	17.2	/	/	/	0.09	0.04	/	/	/
$(17.2\text{-MoHZ-15})_{N2\text{-}700°C}$	13.6	/	/	/	0.01	0.01	/	/	/
$(17.2\text{-MoHZ-15})_{2\ min}$	/	0.2	/	/	0.05	0.01	/	/	/
$(17.2\text{-MoHZ-15})_{5\ min}$	11.5	1.0	/	/	0.02	0.02	/	/	/
$(17.2\text{-MoHZ-15})_{10\ min}$	12.5	1.8	/	/	0.02	0.02	/	/	/
$(17.2\text{-MoHZ-15})_{30\ min}$	12.6	2.5	0.6	/	0.02	0.02	/	/	/
$(17.2\text{-MoHZ-15})_{1\ h}$	12.7	2.4	0.7	/	0.02	0.02	/	6.4	/
$(17.2\text{-MoHZ-15})_{4\ h}$	/	2.2	1.5	/	0.02	0.02	/	12.0	/
$(17.2\text{-MoHZ-15})_{10\ h}$	13.4	1.3	1.1	/	0.02	0.02	/	13.8	/
$(17.2\text{-MoHZ-15})_{20\ h}$	/	1.3	1.3	/	0.02	0.02	/	12.7	/

[a] Mo content measured by ICP analysis, [b] Mo content measured by thermogravimetry analysis, [c] The micropore volume (V_{micro}) is calculated from the t-plot curve using the Harkins-Jura method and a thickness range between 4.5 and 5.5 Å and [d] The mesopore volume (V_{meso}) is the difference between the total pore volume at $P/P_0 = 0.95$ and the micropore volume.

The insoluble coke was subjected to XRD measurements allowing to characterize the molybdenum fate with ToS **(Figure 4**). After 10 min, *i.e.*, during the activation, sharp diffraction peaks at 26.0 °, 37.2 ° and 53.6° ascribed to the [0 0 1], [2 0 0] and [2 2 0] crystal planes of MoO_2 (JCPDS File No. 65-5758) appear.[38] This result clearly shows that MoO_3 located on the zeolite external surface is reduced to MoO_2 during the activation step, then further to molybdenum carbide. This strongly supports previous observations, where MoO_3 carburization is likely to occur in two steps.[39,36] The presence of some MoO_2 peaks after the activation confirms also that complete carburization is not required to produce aromatic compounds.[40]

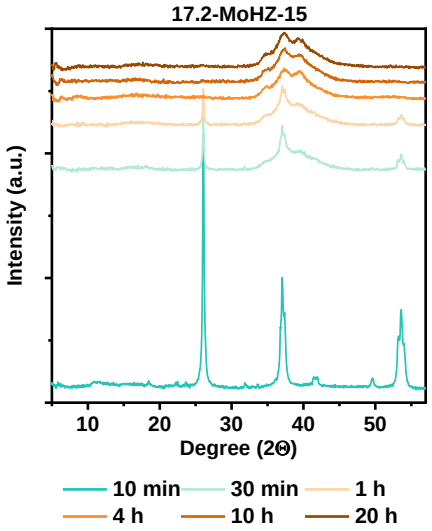

Figure 4: XRD patterns of insoluble coke recovered at different ToS on the 17.2-MoHZ-15 catalyst.

As reaction time increases, new broad peak developed at 2θ = 39.5°, characteristic of β-Mo_2C (JCPDS File No. 35–0787). This large shoulder suggests that molybdenum carbide coexists with amorphous carbon species.[41] Elemental analyses show that the molar C/Mo of the insoluble fraction is about 3.5. By subtracting the carbon measured by TG analysis, the molybdenum carbide composition is MoCx with x ~ 2.5. This value is in good agreement with the oxidation gain observed in the TGA analysis. Beale et al. also proposed that reduced molybdenum species are not indefinitely attached to the Brønsted acid sites and sinter once

the C/Mo molar ratio reaches 3.[42] A picture of coke on the $(17.2\text{-MoHZ-15})_{20h}$ catalyst is shown in **Figure S4**.

4. Modelling deactivation on catalysts 0.9-MoHZ-15 and 2.7-MoHZ-15

The loss of catalyst activity is related to different parameters (ToS, coke content, etc.) according to semi-empirical laws, *vide-infra* and follows the approach outlined by Froment.[34]

Deactivation functions: As shown in **Figure 3.a**, the catalyst deactivation reaches a steady-state of 2% methane conversion after 20 h ToS on both catalysts. The deactivation function, $\phi_k = \frac{r_A}{r_A^0}$ is defined as the ratio between reaction rates of the coked and fresh catalysts (**Eq. 2)** and its time evolution $\phi_k(t) = \exp(-\alpha_t * t)$ (**Eq.3**) contains a deactivation parameter α_t (h^{-1}).[43,44] Such a model does not take into account the experimental conditions.

$\phi_k = \frac{r_A}{r_A^0}$ where | r_a : reaction rate on the coked catalyst; r_a^0: reaction rate on the fresh catalyst; ϕ_k : deactivation function **(Eq. 2)**

$$\phi_k(t) = \exp(-\alpha_t * t) \quad \textbf{(Eq. 3)}$$

This model applied on the 0.9-MoHZ-15 and 2.7-MoHZ-15 catalysts is depicted in **Figure 3.a**. The fitted α_t parameters are α_t (0.9-MoHZ-15) = 0.09 h^{-1} and α_t (2.7-MoHZ-15) = 0.10 h^{-1}, the same order of magnitude as reported elsewhere.[45] Despite different Mo contents, the two deactivation constants are similar, implying that the deactivation is not a function of the Mo located on the external surface of the H-ZSM-5.

The catalyst activity generally depends on coke content (C_t). Since Mo sublimation is negligible on low Mo-containing catalysts (**Table 2**), the deactivation is assumed to be due to coke deposition covering the zeolite acid sites. The first "coke" laid down on the zeolite grow, probably by polymerization and/or poly-condensation, until they block access to the zeolite microporosity.[15,46]

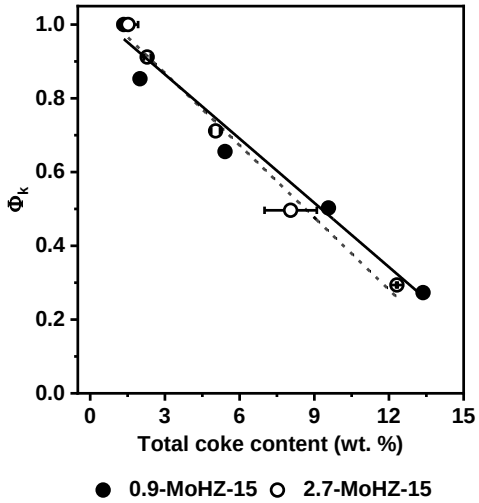

Figure 5: MDA deactivation function on the Mo/HZSM-5 catalyst *vs.* the coke content. Full and dashed lines correspond to catalysts 0.9-MoHZ-15 and 2.7-MoHZ-15, respectively.

The coke content measured by thermal analysis is presented in **Figure 5** for 0.9-MoHZ-15 and 2.7-MoHZ-15 catalysts with a maximum deviation of 10% (based on 4 tests) for the (2.7-MoHZ-15)$_{10h}$ catalyst.

Several empirical functions described by Marin et al. are evaluated.[23] The ($\phi_k(C_t)$) function fits best **(Eq. 3)**, where α_c (wt. %$^{-1}$) is the "coke content" deactivation constant. Similar values are also obtained: α_c(0.9-MoHZ-15) = 0.06 wt%$^{-1}$ and α_c(2.7-MoHZ-15) = 0.07 wt%$^{-1}$.

$$\phi_k(C_t) = 1 - \alpha_c * C_t \qquad \textbf{(Eq. 4)}$$

Coke content is not zero when Φ_k = 1, *i.e.*, at the beginning of the reaction as it is likely to belong to the organo-catalytic complex often referred to as the hydrocarbon pool.[18]

From (**Eq. 2**) and (**Eq. 3**), the total amount of coke deposited during the catalyst lifetime (**Eq. 5**) is estimated:

$$C_t(t) = \frac{1 - \exp(-\alpha_t * t)}{\alpha_c} \qquad (\textbf{Eq. 5})$$

A Taylor expansion of the e^x function close to 0 shows that coke species depend linearly on ToS (**Eq. 6**):

$$\lim_{t\to 0}(c_t) = \frac{\alpha_t}{\alpha_c} * t \qquad \textbf{(Eq. 6)}$$

The combustion of coke deposited at ToS and MS analysis of on-line evolved gas can validate the models.

The coke content as a function of ToS is plotted in **Figure** 6. Coke appears after the activation period and is first detected on the 0.9-MoHZ-15 catalyst with the lowest Mo loading (**Table 2**).

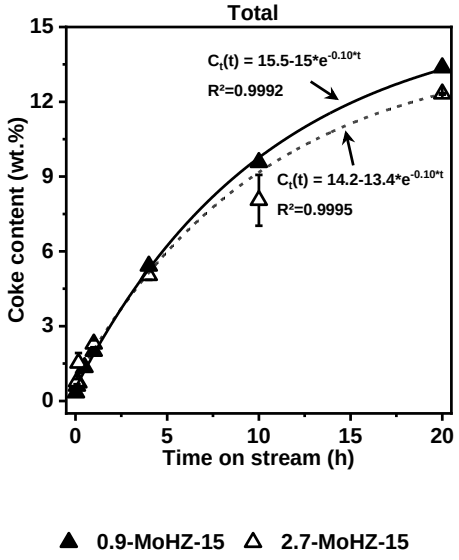

Figure 6: Total coke content as a function of ToS. Full and open symbols correspond to the 0.9-MoHZ-15 and 2.7-MoHZ-15 catalysts, respectively.

These results can be fitted well with the model proposed in **Eq. 5** where the deactivation constants α_t and α_c are related to the total carbon deposition. The recovered coke content fits a negative exponential function with ToS; when the latter nears, the coke content recovered approaches ~ 15 wt. % for both catalysts. The $1/\alpha_c$ constant represents the maximum limit of carbon deposition.

After the activation step, it is possible to assess the solid carbon deposited on the catalyst (Table 2), the total amount of coke recovered on the sample 2.7-MoHZ-15 is 1.5 wt. % and

on the sample 0.9-MoHZ-15 is lower: 0.9 wt.%. In the same operating condition with a catalyst loaded with 6 wt. % of molybdenum Hensen et al. calculated 3.7 wt.%.[15] Thus, as suggested by Iglesia et al., Molybdenum content favor the carbon deposition during the activation step.[10]

Deactivation descriptors representing textural/structural properties of the spent catalysts: Nitrogen physisorption results indicate a loss of microporous volume of deactivated samples as reported earlier.[23] XRD analysis data, less often used in similar studies, indicate potential structural modifications of the zeolites.

Residual micropore volume: The residual micropore volume (V/V_0) of spent catalysts recovered at different ToS is plotted as a function of their coke content (**Figure 7),** where V_0 belongs to a catalyst heated under nitrogen at 700 °C. It indicates that the loss of microporous volume follows the same linear trend as the loss of catalytic activity (**Figure 5)**.

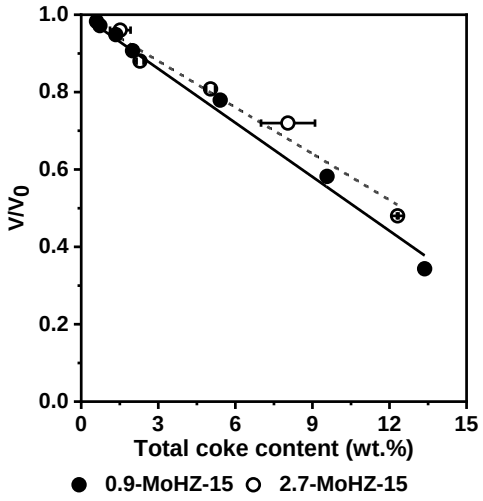

Figure 7: Residual micropore volume (V/V_0) of the 0.9-MoHZ-15 (full line) and 2.7-MoHZ-15 (dashed line) catalysts as a function of the total coke content.

By analogy, a linear function, $(\phi_k(V/V_0))$, can also be derived where α_v is the "remaining microporous volume" deactivation constant:

$$\phi_k\left(\frac{V}{V_0}\right) = 1 - \alpha_v * C_t \qquad \textbf{(Eq. 7)}$$

On both catalysts, α_v are 0.04 (wt% $^{-1}$) indicating that the coke blocks the zeolite micropores, independently of Mo loading. As micropores become ever more inaccessible, carbon species accumulate in the mesopores (**Table 2).** Due to carbon deposition in the mesopores and on the external zeolite surface,[42,47] α_v is slightly lower than α_c.

From orthorhombic to tetragonal structure: XRD features can indicate the impact of coke deposition on the spent catalysts (**Figure 8**). In the 21° - 28° 2θ range, five peaks characteristic of HZSM-5 appear at 23.1°, 23.3°, 23.8°, 24.1, and 24.5°.[48] Throughout the catalyst lifetime, no loss of peak intensity or presence of an amorphous phase is noticed, indicating that the zeolite integrity is kept during the coke deposition. There are also no characteristic peak of graphitic type of coke at 26.8 °.[49] Therefore, a negligible amount of coke is assumed to be deposited on the external surface.

The peak at 23.3° corresponding to the [0 5 1] crystal plane of the HZSM-5 progressively shifts to lower 2Θ till overlaps with the peak at 23.1 ° corresponding to the [5 0 1] crystal plane. This corresponds to the apparent symmetry change from orthorhombic to tetragonal structure[50] caused by the deformation of the MFI pores upon build-up of polyaromatic specie].[51,52-53]

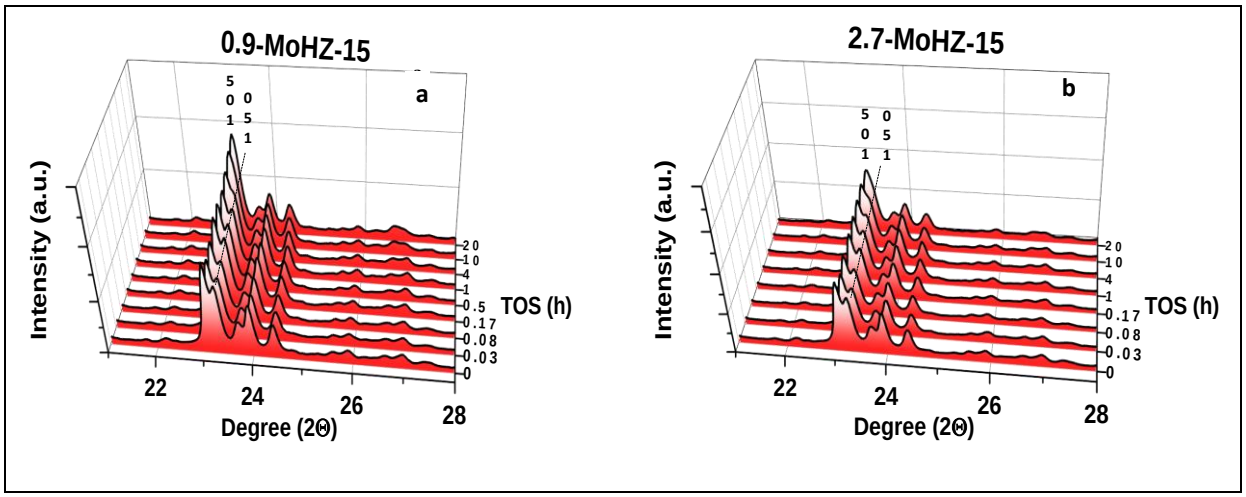

Figure 8: XRD patterns of (a) 0.9-MoHZ-15 and (b) 2.7-MoHZ-15 catalysts as a function of MDA ToS. The blue and black dashed line correspond to the reflection peaks [501] and [051] of the HZSM-5 zeolite, respectively.

The kinetics of this phase transition is complex and not linear. At the beginning, no changes occur till coke exceeds 5 wt. %, (ToS > 4 h). On the 2.7-MoHZ-15 catalyst, a shoulder appears after 10 h ToS and this is less pronounced on 0.9-MoHZ-15. This feature is due to faster coking on a catalyst with a low level of Mo.

A similar behavior of the catalyst evolution by *operando* XRD was observed by Hensen et al. [54] where coke was also located inside the zeolite micropores.[50] They also report that coke accumulation is accompanied by a change in unit cell size, first decreasing during the early stages of the reaction followed by a continuous increase. Thus, the lattice parameter variation (first shrinkage, then expansion) and the difference between a and b unit cell parameters can also be used as deactivation descriptors [[53]]. Additionally, the presence of a peak at 23.3° 2 Theta is also a signature of symmetric change from orthorhombic to tetragonal structure.[[50],[55]] A deconvolution of the peaks in the 23.1°- 23.3° 2 Theta range determines the proportion of the monoclinic phase. As shown in **Figure 9**, the intensity of the 23.3°peak depends on the residual microporous volume. More specifically, the lower the residual microporous volume (the higher the coke recovered), the more pronounced the transition phase. However, for high residual microporous volume (low coke content), it is difficult to estimate the transition phase since a plateau is reached once the residual microporous volume exceeds 70%. Therefore, the change from orthorhombic to tetragonal structure is a deactivation descriptor only if some coke is trapped in the zeolite micropores and not elsewhere.

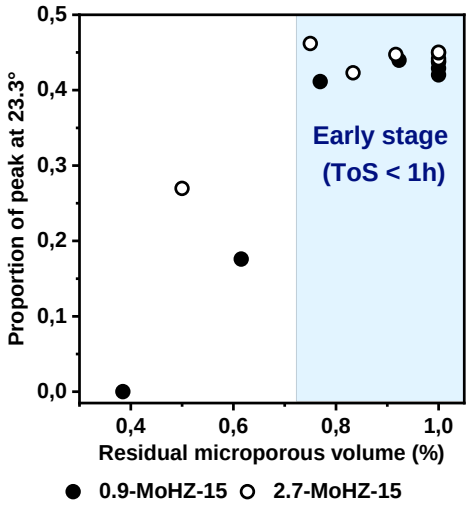

Figure 9: Proportion of the 23.3° 2 Theta peak (monoclinic phase) *vs.* the microporous volume of catalysts 0.9-MoHZ-15 (full symbols) and 2.7-MoHZ-15 (open symbols). The blue area corresponds to the early stage of the reaction for ToS < 1 h.

Presence of molybdenum carbide. Distinguishing "Soft" and "Hard" coke: all spent MDA catalysts display similar weight loss profiles as shown in **Figure S6**. First, a small weight gain from ~ 350 °C up to 500 °C due to the oxidation of $Mo_{2.5}C$ in MoO_3 is observed [56]:

(Eq. 8)

$$MoC_{2.5} + 4\,O_2 \rightarrow MoO_3 + 2.5\,CO_2\ (+14\,\%\ in\ mass) \qquad \textbf{(Eq. 8)}$$

The first weight loss occurs at ~ 550 °C followed by a second at ~ 600 °C. MS analysis of the evolved gases (*e.g.,* CO_2: m/z = 44) associates each weight loss with the corresponding oxidation products. All temperature programmed combustions can be deconvoluted in two well-defined peaks; the first and the second are ascribed to oxidation of "soft" and "hard" coke, respectively **(Figure S6.b).**[15,57] Their contributions are calculated from the area under each peak. CO_2 production during the molybdenum carbide oxidation is not significant and no third CO_2 peak at a lower temperature is observed.

The coke levels increase with ToS, and the combustion is more difficult, as peak maxima shifts to higher temperatures (**Figure 10**). A similar trend was already reported elsewhere.[13,15]

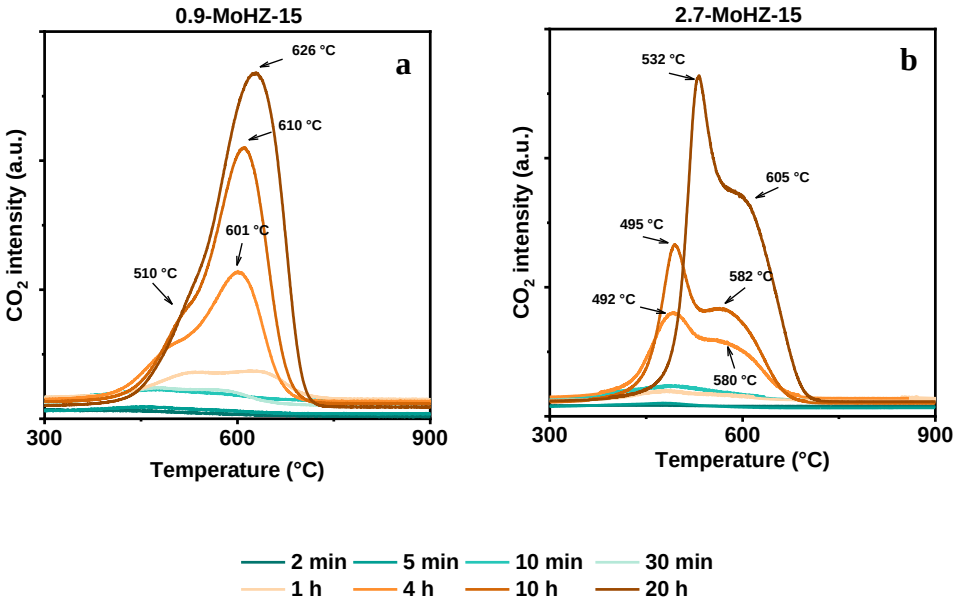

Figure 10: CO_2 evolution during temperature programmed combustion of (a) 0.9-MoHZ-15 and (b) 2.7-MoHZ-15 catalysts recovered at different ToS

By plotting the "soft" and "hard" coke amounts as a function of ToS (**Figure 11.a**) and total coke content **(Figure 11.b)**, two deactivation steps are identified:

- **TOS < 1 h**: before the end of the induction period, coke deposition is independent of Mo loading and a linear correlation appears between coke and ToS giving a total coke formation rate of $k_{coke}^{total} = 1.17\ mmolC\ g_{cat}^{-1}\ h^{-1}$. Under these conditions, the experimental data **are well fitted by Eq. 5**. **Figure 8.b** highlights that "soft" coke appears at low coke content (*i.e.*, early stages of the reaction) and short ToS. Afterwards, "hard" coke emerges and can be quantified. No molybdenum carbide oxidation is detected during this step.

- **TOS > 1 h**: notable changes occur as the initial coke is reduced. The "hard" coke species grow linearly whereas the "soft" coke species level at a maximum value (**Figure 8**). The contribution of "hard" coke increases progressively with ToS, making it more difficult to oxidize. The two catalysts behave differently as more carbon is deposited on the 0.9-MoHZ-15 catalyst. Since it possesses more BAS after the Mo impregnation, coke precursors formation is promoted.[58] A change in the type of coke is also observed (**Figure 8.a**) as "hard" coke is predominant at lower Mo levels, *i.e.*, on the 0.9-MoHZ-15 catalyst. At higher Mo

loading (2.7-MoHZ-15 catalyst), the “soft” coke increases. However, the contribution of “soft” and “hard” coke depends only on the total coke content represented in **Figure 8.b**. Since 2.7-MoHZ-15 contains less coke, its “hard” coke proportion is lower than on 0.9-MoHZ-15. This question the discrepancy between “soft” and ”hard” coke, assumed to be due to a closer intimacy with Mo-reduced moieties catalyzing coke combustion.[19]

The amount of $MoC_{2.5}$ (green symbol, **Eq. 8**) increases with ToS on both catalysts (**Figure 11**). Since it has been established that no MoO_3 is present on the external surface of 0.9-MoHZ-15 catalyst after the calcination step. The appearance and increase of the molybdenum carbide at the external surface suggests a progressively sintering and migration of Mo species throughout the catalyst lifetime (**Figure 11**). Our results are consistent with the recent report by Beale et al. in which the molybdenum reduced moieties detached from their anchoring point once the reaction has started.[42,17] It is possible to estimate the amount of molybdenum that sinter toward the external zeolite surface by knowing the carbide oxidation weight from the TGA analysis: ~ 50% of the initially dispersed molybdenum active site precursors inside the zeolite have migrated after 20 hours of reaction. This proposed value is also close to the 70% of molybdenum sintering reported by the another group.[17]

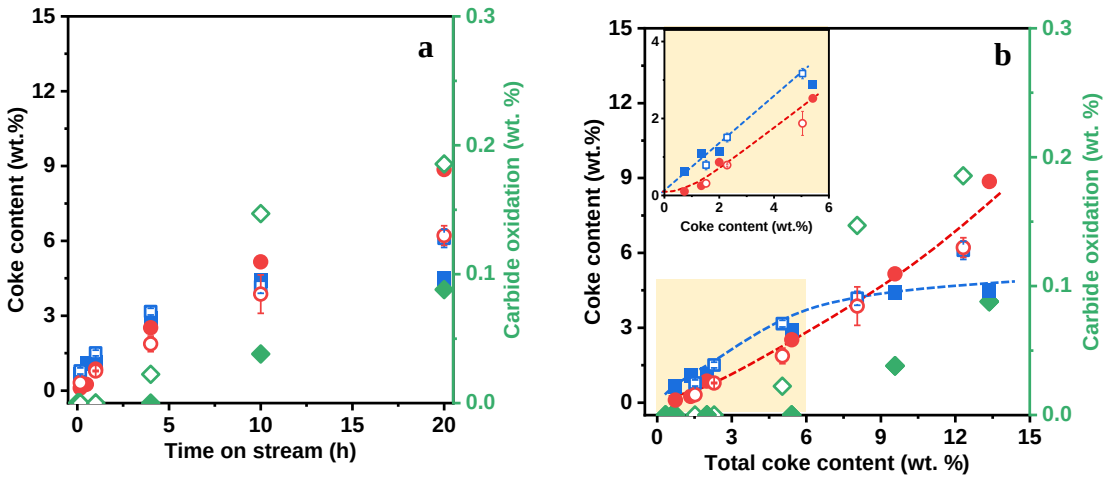

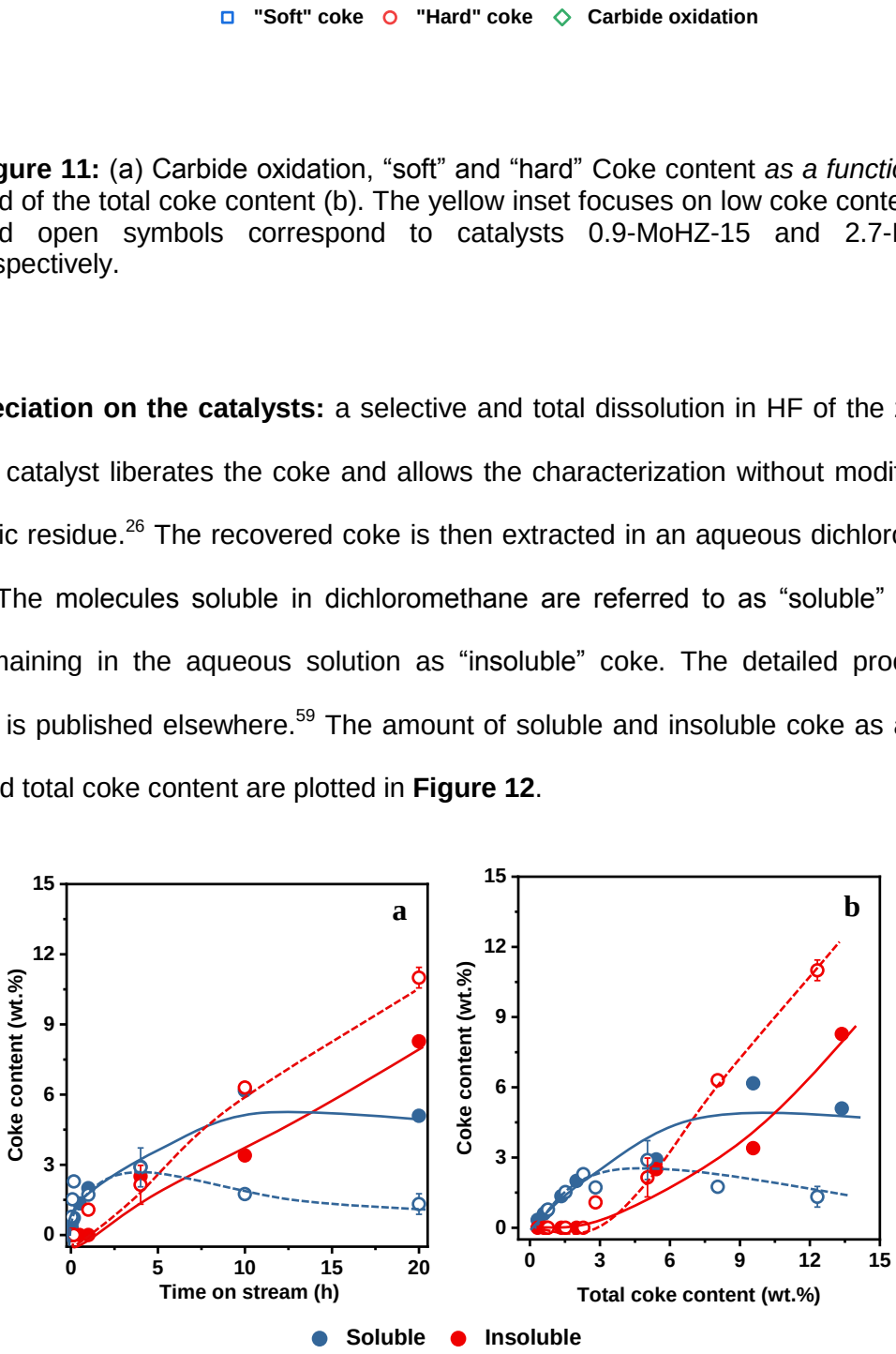

Figure 11: (a) Carbide oxidation, “soft” and “hard” Coke content *as a function of* ToS and of the total coke content (b). The yellow inset focuses on low coke content. D Full and open symbols correspond to catalysts 0.9-MoHZ-15 and 2.7-MoHZ-15, respectively.

Coke speciation on the catalysts: a selective and total dissolution in HF of the zeolite on the spent catalyst liberates the coke and allows the characterization without modification of the organic residue.[26] The recovered coke is then extracted in an aqueous dichloromethane solution. The molecules soluble in dichloromethane are referred to as “soluble” coke and those remaining in the aqueous solution as “insoluble” coke. The detailed procedure of treatment is published elsewhere.[59] The amount of soluble and insoluble coke as a function of ToS and total coke content are plotted in **Figure 12**.

Figure 12: Amount of soluble (blue symbols) and insoluble coke (red symbols) in dichloromethane as a function of ToS and total coke content formed during the MDA reaction. The full line/close symbols and dashed line/open symbols correspond to the fitting of 0.9-MoHZ-15 and 2.7-MoHZ-15 catalysts.

Regardless of Mo loading, the amount of soluble coke goes through a maximum and then decreases as insoluble coke appears. The insoluble coke then increases linearly with the

total coke content. The soluble coke is analyzed by GC-MS (**Figure S7**), and the molecules identified with the appearance time are summarized in **Table S1**; their skeletal formulas are given in **Table S2.** Mainly non-alkyled polyaromatics (pyrene, benzo-pyrene, fluoranthene) are identified in the soluble fraction. These results are consistent with the zeolite MFI framework and the high temperature as reported elsewhere.[60] During the early stages of the reaction (ToS < 1h), alkyl benzenes are recovered from both catalysts. After 1 h, polyaromatics rapidly emerge and their appearance coincides with the end of the induction period (*i.e.*, maximum benzene production),which is in a good agreement with the proposed sp^2 carbon aromatic nature of the coke recently reported.[19] As ToS increases, the degree of aromaticity increases too. On the spent 0.9-MoHZ-15 catalyst, heavier aromatics as benzopyrene are detected while they are absent from sample 2.7-MoHZ-15. Since the micropores of zeolite catalysts are still accessible, the coke combustion is not limited by O_2 diffusion but driven by the aromaticity degree, which explains the higher combustion temperature on the spent 0.9-MoHZ-15 catalyst (**Figure 10)** and the direct relation observed between “soft”/”hard” coke species and total coke recovered (**Figure 11**).

Light polyaromatics are also extracted from the 2.7-MoHZ-15 spent catalyst. Despite N_2 flushing during the cooling down of the reactor, naphthalene derivatives, produced during the reaction, are detected on 2.7-MoHZ-15 catalyst after several hours of reaction. Molybdenum seems therefore to adsorb light polyaromatics and prevent further polycondensation, supporting our previous assumption that some of the products could be adsorbed on molybdenum-reduced species.[57] This polycondensation is believed to accur at longer ToS, forming a connected structure inside the zeolite channels. After HF extraction, due to their high aromaticity, they remain insoluble and appear as ZTC structures (Zeolite templated carbon).[6,19]

The extracted insoluble coke deposited at different ToS is analyzed by XRD (**Figure S8**); The XRD data show the presence of graphene stacking and therefore the formation of some carbon among the insoluble coke.[61] The broad peak centred around $2\Theta = 22\ °$ highlights its

amorphous structure and no peak characteristic of an ordered carbon structure is observed in any sample.[62] This result is in line with the role frameworks that play in the synthesis of well-defined ZTC materials. In particular, 10-membered ring zeolites are unable to promote the formation carbon-ordered structures due to their narrow pore aperture (*ca.* 0.5 nm) as shown earlier.[62,63]

Conclusions

We highlight three different deactivation modes of MDA catalysts including (i) zeolite amorphization, (ii) coke accumulation inside the micropore, and (iii) carbide migration toward the external surface. The first mode is irreversible since the extra-framework species, $Al_2(MoO_4)_3$, are highly stable and at high Mo loading, lead to the collapse of the zeolite structure at the earliest stage of the catalyst preparation, *i.e.*, during an inert pre-treatment at 700 °C. Such catalysts do not display any activity. It is therefore critical to carefully tune the pre-treatment conditions of catalysts at high Mo loading.

At optimized Mo loading, the catalysts become less sensitive to the pre-treatment and the MDA catalysts still deactivate but very importantly by the two reversible modes. If catalytic processes like MDA should stand a chance of industrial deployment, any rapid and irreversible deactivation should be avoided. We modelled the deactivation kinetics independently of the Mo content of the catalysts and the loss of catalytic activity is found to follow an exponential decay with time on stream and a linear decay with coke level. This suggests that coke progressively fills the zeolite micropores, blocking access to the active sites.

Two different coking processes take place:

(i) During the induction period (< 1 h), coke formation is independent of the Mo loading. It corresponds to the building-up of a hydrocarbon pool inside the zeolite channels. Coke extraction provides for the first time a direct insight on its composition. Unsubstituted

polyaromatics traditionally recovered on MFI type framework at high temperature constitute this organo-catalytic complex.

(ii) After a maximum in benzene production is reached (> 1 h), lighter coke grows into heavier coke accumulating in the zeolite micropores leading to their progressive blocking. Afterwards, the coke fills the mesopores of zeolite catalysts. The coke growth appears to depend on Mo loading since it prevents the formation of compounds with higher aromaticity degrees. However, molybdenum-reduced centers move to the external surface where they sinter as molybdenum carbides. At least 50% of the initially well dispersed molybdenum moieties end up on the external surface of the zeolite crystals after 20 h of reaction.

The coke recovered on the catalyst is a descriptor of catalytic activity loss in the MDA reaction. The accumulation of coke on the catalyst initiates changes of its textural and structural properties. From these modifications, two other deactivation descriptors could be derived: (i) the remaining microporous volume on spent catalysts since coke mainly accumulates in the zeolite micropores where the reaction occurs, and (ii) the monoclinic to orthorhombic zeolite phase transition, a descriptor of coke growth in the micropores, *i.e.*, the nature of coke.

HF extraction of coke from spent catalysts followed by GC-MS confirms that coking is a shape-selective process at high temperatures and the formation of the hydrocarbon pool is driven by the zeolite microporosity. This feature highlights that some ten-membered ring zeolites (MFI, MWW) perform better in the MDA process.

As coke deposition and carbide migration both lead to only reversible deactivation, selecting the optimal conditions for catalyst regeneration and subsequent re-carburization of the active sites (avoiding irreversible Al extraction followed aluminum molybdates formation) are required for any potential MDA process industrialization. In that regard, further attention to series-flow reactors with dedicated monofunctional catalysts each working under different optimized conditions is highly desired as irreversible deactivation can be avoided and coking could take place under mild conditions.[64]

Acknowledgments

The authors acknowledge financial support from the European Union (ERDF) and “Région Nouvelle Aquitaine”.

A. Beuque, and L. Pinard thank the European Union’s Horizon 2020 research and innovation program for its funding under grant agreement No 814548. This publication only reflects the author’s views, and neither Agency nor the Commission is responsible for any use that may be made of the information contained therein.

L. Pinard thanks the Region Normandie for funding the BioDNH “Chaire d’Excellence”.

References:

(1) Amghizar, I.; Vandewalle, L. A.; Van Geem, K. M.; Marin, G. B. New Trends in Olefin Production. *Engineering* **2017**, *3* (2), 171–178. https://doi.org/10.1016/J.ENG.2017.02.006.

(2) International Energy Agency. *Tracking Clear Energy Progress 2017*; 2017.

(3) Song, H.; Jarvis, J.; Meng, S.; Xu, H.; Li, Z.; Li, W. Introducing Methane Activation. In *Methane Activation and Utilization in the Petrochemical and Biofuel Industries*; Song, H., Jarvis, J., Meng, S., Xu, H., Li, Z., Li, W., Eds.; Springer International Publishing: Cham, 2022; pp 23–41. https://doi.org/10.1007/978-3-030-88424-6_2.

(4) Tang, P.; Zhu, Q.; Wu, Z.; Ma, D. Methane Activation: The Past and Future. *Energy Environ. Sci.* **2014**, *7* (8), 2580–2591. https://doi.org/10.1039/C4EE00604F.

(5) Bao, J.; Yang, G.; Yoneyama, Y.; Tsubaki, N. Significant Advances in C1 Catalysis: Highly Efficient Catalysts and Catalytic Reactions. *ACS Catal.* **2019**, *9* (4), 3026–3053. https://doi.org/10.1021/acscatal.8b03924.

(6) Kosinov, N.; Hensen, E. J. M. Reactivity, Selectivity, and Stability of Zeolite-Based Catalysts for Methane Dehydroaromatization. *Advanced Materials* **2020**, *32* (44), 2002565. https://doi.org/10.1002/adma.202002565.

(7) Ma, S.; Guo, X.; Zhao, L.; Scott, S.; Bao, X. Recent Progress in Methane Dehydroaromatization: From Laboratory Curiosities to Promising Technology. *Journal of Energy Chemistry* **2013**, *22* (1), 1–20. https://doi.org/10.1016/S2095-4956(13)60001-7.

(8) Cruchade, H.; Medeiros-Costa, I. C.; Nesterenko, N.; Gilson, J.-P.; Pinard, L.; Beuque, A.; Mintova, S. Catalytic Routes for Direct Methane Conversion to Hydrocarbons and Hydrogen: Current State and Opportunities. *ACS Catal.* **2022**, *12* (23), 14533–14558. https://doi.org/10.1021/acscatal.2c03747.

(9) Tan, P. L.; Leung, Y. L.; Lai, S. Y. The Effect of Calcination Temperature on the Catalytic Performance of 2 Wt.% Mo/HZSM-5 in Methane Aromatization. *Applied Catalysis A: General* **2002**, *228*, 115–125. https://doi.org/10.1016/S0926-860X(01)00955-3.

(10) Kim, Y.-H.; Borry, R. W.; Iglesia, E. Genesis of Methane Activation Sites in Mo-Exchanged H–ZSM-5 Catalysts. *Microporous and Mesoporous Materials* **2000**, *35–36*, 495–509. https://doi.org/10.1016/S1387-1811(99)00245-0.
(11) Clatworthy, E. B.; Konnov, S. V.; Dubray, F.; Nesterenko, N.; Gilson, J.-P.; Mintova, S. Emphasis on the Properties of Metal-Containing Zeolites Operating Outside the Comfort Zone of Current Heterogeneous Catalytic Reactions. *Angewandte Chemie* **2020**, *n/a* (n/a). https://doi.org/10.1002/ange.202005498.
(12) Vollmer, I.; Yarulina, I.; Kapteijn, F.; Gascon, J. Progress in Developing a Structure-Activity Relationship for the Direct Aromatization of Methane. *ChemCatChem* **2019**, *11* (1), 39–52. https://doi.org/10.1002/cctc.201800880.
(13) Song, Y.; Xu, Y.; Suzuki, Y.; Nakagome, H.; Zhang, Z.-G. A Clue to Exploration of the Pathway of Coke Formation on Mo/HZSM-5 Catalyst in the Non-Oxidative Methane Dehydroaromatization at 1073K. *Applied Catalysis A: General* **2014**, *482*, 387–396. https://doi.org/10.1016/j.apcata.2014.06.018.
(14) Song, Y.; Xu, Y.; Suzuki, Y.; Nakagome, H.; Ma, X.; Zhang, Z.-G. The Distribution of Coke Formed over a Multilayer Mo/HZSM-5 Fixed Bed in H2 Co-Fed Methane Aromatization at 1073K: Exploration of the Coking Pathway. *Journal of Catalysis* **2015**, *330*, 261–272. https://doi.org/10.1016/j.jcat.2015.07.017.
(15) Tempelman, C.; Hensen, E. J. M. On the Deactivation of Mo/HZSM-5 in the Methane Dehydroaromatization Reaction. *Applied Catalysis B: Environmental* **2015**, *176–177*, 731–739. https://doi.org/10.1016/j.apcatb.2015.04.052.
(16) Wang, N.; Dong, X.; Liu, L.; Cai, D.; Cheng, Q.; Wang, J.; Hou, Y.; Emwas, A.-H.; Gascon, J.; Han, Y. Probing the Catalytic Active Sites of Mo/HZSM-5 and Their Deactivation during Methane Dehydroaromatization. *Cell Reports Physical Science* **2021**, *2* (1), 100309. https://doi.org/10.1016/j.xcrp.2020.100309.
(17) Beale, A. M.; Agote-Aran, M.; Lezcano-Gonzalez, I. Determination of Molybdenum Species Evolution during Non-Oxidative Dehydroaromatization of Methane and Its Implications for Catalytic Performance. *ChemCatChem* **2019**, *11* (1), 473–480.
(18) Kosinov, N.; Hensen, E. J. M.; Uslamin, E. A. Confined Carbon Mediating Dehydroaromatization of Methane over Mo/ZSM-5. *Angewandte Chemie International Edition* **2018**, *57* (4), 1016–1020.
(19) Kosinov, N.; Uslamin, E. A.; Coumans, F. J. A. G.; Wijpkema, A. S. G.; Rohling, R. Y.; Hensen, E. J. M. Structure and Evolution of Confined Carbon Species during Methane Dehydroaromatization over Mo/ZSM-5. *ACS Catal.* **2018**, *8* (9), 8459–8467. https://doi.org/10.1021/acscatal.8b02491.
(20) Gu, Y.; Chen, P.; Yan, H.; Wang, X.; Lyu, Y.; Tian, Y.; Liu, W.; Yan, Z.; Liu, X. Coking Mechanism of Mo/ZSM-5 Catalyst in Methane Dehydroaromatization. *Applied Catalysis A: General* **2021**, *613*, 118019. https://doi.org/10.1016/j.apcata.2021.118019.
(21) Vollmer, I.; Kosinov, N.; Szécsényi, Á.; Li, G.; Yarulina, I.; Abou-Hamad, E.; Gurinov, A.; Ould-Chikh, S.; Aguilar-Tapia, A.; Hazemann, J.-L.; Pidko, E.; Hensen, E.; Kapteijn, F.; Gascon, J. A Site-Sensitive Quasi-in Situ Strategy to Characterize Mo/HZSM-5 during Activation. *Journal of Catalysis* **2019**, *370*, 321–331. https://doi.org/10.1016/j.jcat.2019.01.013.
(22) Guisnet, M.; Magnoux, P. Organic Chemistry of Coke Formation. *Applied Catalysis A: General* **2001**, *212* (1), 83–96. https://doi.org/10.1016/S0926-860X(00)00845-0.
(23) Reyniers, M.-F.; Thybaut, J. W.; Marin, G. B. MODELLING OF DEACTIVATION BY COKE FORMATION. In *Deactivation and Regeneration of Zeolite Catalysts*; IMPERIAL COLLEGE PRESS, 2011; Vol. 9, pp 151–169. https://doi.org/10.1142/9781848166387_0009.
(24) Beuque, A.; Hao, H.; Berrier, E.; Sachse, A.; Paul, J.-F.; Pinard, L. How Does the Balance of Metal and Acid Functions on the Benchmark Mo/ZSM-5 Catalyst Drive the Methane Dehydroaromatization Reaction? *Catalysis Today* **2022**. https://doi.org/10.1016/j.cattod.2022.06.001.

(25) Xu, Y.; Lin, L. Recent Advances in Methane Dehydro-Aromatization over Transition Metal Ion-Modified Zeolite Catalysts under Non-Oxidative Conditions. *Applied Catalysis A: General* **1999**, *188* (1), 53–67. https://doi.org/10.1016/S0926-860X(99)00210-0.

(26) Magnoux, P.; Roger, P.; Canaff, C.; Fouche, V.; Gnep, N. S.; Guisnet, M. New Technique for the Characterization of Carbonaceous Compounds Responsible for Zeolite Deactivation. In *Studies in Surface Science and Catalysis*; Delmon, B., Froment, G. F., Eds.; Catalyst Deactivation 1987; Elsevier, 1987; Vol. 34, pp 317–330. https://doi.org/10.1016/S0167-2991(09)60370-0.

(27) Ding, Q. P.; Huang, H. B.; Duan, J. H.; Gong, J. F.; Yang, S. G.; Zhao, X. N.; Du, Y. W. Molybdenum Trioxide Nanostructures Prepared by Thermal Oxidization of Molybdenum. *Journal of Crystal Growth* **2006**, *294* (2), 304–308. https://doi.org/10.1016/j.jcrysgro.2006.07.004.

(28) López-Martín, Á.; Caballero, A.; Colón, G. Unraveling the Mo/HZSM-5 Reduction Pre-Treatment Effect on Methane Dehydroaromatization Reaction. *Applied Catalysis B: Environmental* **2022**, *312*, 121382. https://doi.org/10.1016/j.apcatb.2022.121382.

(29) Haro-Poniatowski, E.; Jouanne, M.; Morhange, J. F.; Julien, C.; Diamant, R.; Fernández-Guasti, M.; Fuentes, G. A.; Alonso, J. C. Micro-Raman Characterization of WO3 and MoO3 Thin Films Obtained by Pulsed Laser Irradiation. *Applied Surface Science* **1998**, *127–129*, 674–678. https://doi.org/10.1016/S0169-4332(97)00724-1.

(30) Plazenet, G.; Payen, E.; Lynch, J.; Rebours, B. Study by EXAFS, Raman, and NMR Spectroscopies of the Genesis of Oxidic Precursors of Zeolite-Supported HDS Catalysts. *J. Phys. Chem. B* **2002**, *106* (28), 7013–7028. https://doi.org/10.1021/jp020538m.

(31) Tian, H.; Roberts, C. A.; Wachs, I. E. Molecular Structural Determination of Molybdena in Different Environments: Aqueous Solutions, Bulk Mixed Oxides, and Supported MoO3 Catalysts. *J. Phys. Chem. C* **2010**, *114* (33), 14110–14120. https://doi.org/10.1021/jp103269w.

(32) Kosinov, N.; Coumans, F. J. a. G.; Li, G.; Uslamin, E. A.; Mezari, B.; Wijpkema, A. S. G.; Pidko, E. A.; Hensen, E. J. M. Stable Mo/HZSM-5 Methane Dehydroaromatization Catalysts Optimized for High-Temperature Calcination-Regeneration. *Journal of Catalysis* **2017**, *346*. https://doi.org/10.1016/j.jcat.2016.12.006.

(33) Zhang, W.; Ma, D.; Han, X.; Liu, X.; Bao, X.; Guo, X.; Wang, X. Methane Dehydro-Aromatization over Mo/HZSM-5 in the Absence of Oxygen: A Multinuclear Solid-State NMR Study of the Interaction between Supported Mo Species and HZSM-5 Zeolite with Different Crystal Sizes. *Journal of Catalysis* **1999**, *188* (2), 393–402. https://doi.org/10.1006/jcat.1999.2670.

(34) Borry, R. W.; Kim, Y. H.; Huffsmith, A.; Reimer, J. A.; Iglesia, E. Structure and Density of Mo and Acid Sites in Mo-Exchanged H-ZSM5 Catalysts for Nonoxidative Methane Conversion. *J. Phys. Chem. B* **1999**, *103* (28), 5787–5796. https://doi.org/10.1021/jp990866v.

(35) Tessonnier, J.-P.; Louis, B.; Rigolet, S.; Ledoux, M. J.; Pham-Huu, C. Methane Dehydro-Aromatization on Mo/ZSM-5: About the Hidden Role of Brønsted Acid Sites. *Applied Catalysis A: General* **2008**, *336* (1), 79–88. https://doi.org/10.1016/j.apcata.2007.08.026.

(36) Rahman, M.; Infantes-Molina, A.; Boubnov, A.; Bare, S. R.; Stavitski, E.; Sridhar, A.; Khatib, S. J. Increasing the Catalytic Stability by Optimizing the Formation of Zeolite-Supported Mo Carbide Species Ex Situ for Methane Dehydroaromatization. *Journal of Catalysis* **2019**, *375*, 314–328. https://doi.org/10.1016/j.jcat.2019.06.002.

(37) Sridhar, A.; Rahman, M.; Infantes-Molina, A.; Wylie, B. J.; Borcik, C. G.; Khatib, S. J. Bimetallic Mo-Co/ZSM-5 and Mo-Ni/ZSM-5 Catalysts for Methane Dehydroaromatization: A Study of the Effect of Pretreatment and Metal Loadings on the Catalytic Behavior. *Applied Catalysis A: General* **2020**, *589*, 117247. https://doi.org/10.1016/j.apcata.2019.117247.

(38) Zhang, H.-J.; Shu, J.; Wang, K.-X.; Chen, X.-T.; Jiang, Y.-M.; Wei, X.; Chen, J.-S. Lithiation Mechanism of Hierarchical Porous MoO 2 Nanotubes Fabricated through One-Step Carbothermal Reduction. *Journal of Materials Chemistry A* **2014**, *2* (1), 80–86. https://doi.org/10.1039/C3TA14123C.

(39) Ma, D.; Shu, Y.; Cheng, M.; Xu, Y.; Bao, X. On the Induction Period of Methane Aromatization over Mo-Based Catalysts. *Journal of Catalysis* **2000**, *194* (1), 105–114. https://doi.org/10.1006/jcat.2000.2908.
(40) Ma, D.; Shu, Y.; Bao, X.; Xu, Y. Methane Dehydro-Aromatization under Nonoxidative Conditions over Mo/HZSM-5 Catalysts: EPR Study of the Mo Species on/in the HZSM-5 Zeolite. *Journal of Catalysis* **2000**, *189* (2), 314–325. https://doi.org/10.1006/jcat.1999.2704.
(41) Liang, P.; Gao, H.; Yao, Z.; Jia, R.; Shi, Y.; Sun, Y.; Fan, Q.; Wang, H. Simple Synthesis of Ultrasmall β-Mo2C and α-MoC1−x Nanoparticles and New Insights into Their Catalytic Mechanisms for Dry Reforming of Methane. *Catal. Sci. Technol.* **2017**, *7* (15), 3312–3324. https://doi.org/10.1039/C7CY00708F.
(42) Lezcano-González, I.; Oord, R.; Rovezzi, M.; Glatzel, P.; Botchway, S. W.; Weckhuysen, B. M.; Beale, A. M. Molybdenum Speciation and Its Impact on Catalytic Activity during Methane Dehydroaromatization in Zeolite ZSM-5 as Revealed by Operando X-Ray Methods. *Angewandte Chemie* **2016**, *128* (17), 5301–5305. https://doi.org/10.1002/ange.201601357.
(43) Marin, G. B.; Froment, G. F. Reforming of C6 Hydrocarbons on a Pt□Al2O3 Catalyst. *Chemical Engineering Science* **1982**, *37* (5), 759–773. https://doi.org/10.1016/0009-2509(82)85037-9.
(44) Levenspiel, O. Experimental Search for a Simple Rate Equation to Describe Deactivating Porous Catalyst Particles. *Journal of Catalysis* **1972**, *25* (2), 265–272. https://doi.org/10.1016/0021-9517(72)90227-8.
(45) Rahman, M.; Infantes-Molina, A.; Hoffman, A. S.; Bare, S. R.; Emerson, K. L.; Khatib, S. J. Effect of Si/Al Ratio of ZSM-5 Support on Structure and Activity of Mo Species in Methane Dehydroaromatization. *Fuel* **2020**, *278*, 118290. https://doi.org/10.1016/j.fuel.2020.118290.
(46) Song, Y.; Zhang, Q.; Xu, Y.; Zhang, Y.; Matsuoka, K.; Zhang, Z.-G. Coke Accumulation and Deactivation Behavior of Microzeolite-Based Mo/HZSM-5 in the Non-Oxidative Methane Aromatization under Cyclic CH4-H2 Feed Switch Mode. *Applied Catalysis A: General* **2017**, *530*, 12–20. https://doi.org/10.1016/j.apcata.2016.11.016.
(47) Ma, D.; Wang, D.; Su, L.; Shu, Y.; Xu, Y.; Bao, X. Carbonaceous Deposition on Mo/HMCM-22 Catalysts for Methane Aromatization: A TP Technique Investigation. *Journal of Catalysis* **2002**, *208* (2), 260–269. https://doi.org/10.1006/jcat.2002.3540.
(48) Al-Dughaither, A. S.; de Lasa, H. HZSM-5 Zeolites with Different SiO2/Al2O3 Ratios. Characterization and NH3 Desorption Kinetics. *Ind. Eng. Chem. Res.* **2014**, *53* (40), 15303–15316. https://doi.org/10.1021/ie4039532.
(49) Jang, J. Y.; Kim, M. S.; Jeong, H. M.; Shin, C. M. Graphite Oxide/Poly(Methyl Methacrylate) Nanocomposites Prepared by a Novel Method Utilizing Macroazoinitiator. *Composites Science and Technology* **2009**, *69* (2), 186–191. https://doi.org/10.1016/j.compscitech.2008.09.039.
(50) Rojo-Gama, D.; Nielsen, M.; Wragg, D. S.; Dyballa, M.; Holzinger, J.; Falsig, H.; Lundegaard, L. F.; Beato, P.; Brogaard, R. Y.; Lillerud, K. P.; Olsbye, U.; Svelle, S. A Straightforward Descriptor for the Deactivation of Zeolite Catalyst H-ZSM-5. *ACS Catal.* **2017**, *7* (12), 8235–8246. https://doi.org/10.1021/acscatal.7b02193.
(51) Yeong Gim, M.; Hyun Lim, Y.; Lee, K.-Y.; Heui Kim, D. Coaromatization of Methane and Propane over Ga Supported on HZSM-5 Catalysts: The Effect of Mesoporosity on Deactivation Behavior. *Fuel* **2021**, *304*, 121497. https://doi.org/10.1016/j.fuel.2021.121497.
(52) Ardit, M.; Martucci, A.; Cruciani, G. Monoclinic–Orthorhombic Phase Transition in ZSM-5 Zeolite: Spontaneous Strain Variation and Thermodynamic Properties. *J. Phys. Chem. C* **2015**, *119* (13), 7351–7359. https://doi.org/10.1021/acs.jpcc.5b00900.
(53) N. Kalantzopoulos, G.; Gama, D. R.; K. Pappas, D.; Dovgaliuk, I.; Olsbye, U.; Beato, P.; F. Lundegaard, L.; S. Wragg, D.; Svelle, S. Real-Time Regeneration of a Working Zeolite Monitored via Operando X-Ray Diffraction and Crystallographic Imaging: How Coke Flees the MFI Framework. *Dalton Transactions* **2022**, *51* (44), 16845–16851. https://doi.org/10.1039/D2DT02845J.
(54) Liu, Y.; Zhang, H.; Wijpkema, A. S. G.; Coumans, F. J. A. G.; Meng, L.; Uslamin, E. A.; Longo, A.; Hensen, E. J. M.; Kosinov, N. Understanding the Preparation and Reactivity of Mo/ZSM-5

Methane Dehydroaromatization Catalysts. *Chemistry – A European Journal* **2022**, *28* (5), e202103894. https://doi.org/10.1002/chem.202103894.
(55) Alvarez, A. G.; Viturro, H.; Bonetto, R. D. Structural Changes on Deactivation of ZSM-5. A Study by X-Ray Powder Diffraction. *Materials Chemistry and Physics* **1992**, *32* (2), 135–140. https://doi.org/10.1016/0254-0584(92)90269-E.
(56) Liu, H.; Li, T.; Tian, B.; Xu, Y. Study of the Carbonaceous Deposits Formed on a Mo/HZSM-5 Catalyst in Methane Dehydro-Aromatization by Using TG and Temperature-Programmed Techniques. *Applied Catalysis A: General* **2001**, *213* (1), 103–112. https://doi.org/10.1016/S0926-860X(00)00883-8.
(57) Beuque, A.; Hao, H.; Berrier, E.; Batalha, N.; Sachse, A.; Paul, J.-F.; Pinard, L. How Do the Products in Methane Dehydroaromatization Impact the Distinct Stages of the Reaction? *Applied Catalysis B: Environmental* **2022**, *309*, 121274. https://doi.org/10.1016/j.apcatb.2022.121274.
(58) Martínez, A.; Peris, E.; Vidal-Moya, A. Modulation of Zeolite Acidity by Post-Synthesis Treatments in Mo/HZSM-5 Catalysts for Methane Dehydroaromatization. *Studies in Surface Science and Catalysis* **2008**, *174*, 1075–1080. https://doi.org/10.1016/S0167-2991(08)80072-9.
(59) Guisnet, M.; Costa, L.; Ribeiro, F. R. Prevention of Zeolite Deactivation by Coking. *Journal of Molecular Catalysis A: Chemical* **2009**, *305* (1), 69–83. https://doi.org/10.1016/j.molcata.2008.11.012.
(60) Guisnet, M.; Magnoux, P. Fundamental Description of Deactivation and Regeneration of Acid Zeolites. In *Studies in Surface Science and Catalysis*; Delmon, B., Froment, G. F., Eds.; Catalyst Deactivation 1994; Elsevier, 1994; Vol. 88, pp 53–68. https://doi.org/10.1016/S0167-2991(08)62729-9.
(61) Liu, Y.; Osta, E. H.; Poryvaev, A. S.; Fedin, M. V.; Longo, A.; Nefedov, A.; Kosinov, N. Direct Conversion of Methane to Zeolite-Templated Carbons, Light Hydrocarbons, and Hydrogen. *Carbon* **2023**, *201*, 535–541. https://doi.org/10.1016/j.carbon.2022.09.050.
(62) Nishihara, H.; Kyotani, T. Zeolite-Templated Carbons – Three-Dimensional Microporous Graphene Frameworks. *Chem. Commun.* **2018**, *54* (45), 5648–5673. https://doi.org/10.1039/C8CC01932K.
(63) Aumond, T.; Esteves, M.; Pouilloux, Y.; Faccio, R.; Sachse, A. Impact of the Crystal Size of Beta Zeolite on the Structural Quality of Zeolite Templated Carbons. *Microporous and Mesoporous Materials* **2022**, *331*, 111644. https://doi.org/10.1016/j.micromeso.2021.111644.
(64) Konnov, S. V.; Medeiros-Costa, I. C.; Cruchade, H.; Dubray, F.; Debost, M.; Gilson, J.-P.; Valtchev, V.; Dath, J.-P.; Nesterenko, N.; Mintova, S. Formulation of Two Monofunctionnal Catalysts for CH4 Upgrading. *Applied Catalysis A: General* **2022**, 118814. https://doi.org/10.1016/j.apcata.2022.118814.

Supporting Information

Table and figures

Table S1: Coke molecules of the soluble fraction identified by GC-MS

Table S2: Skeletal formula of the coke molecules present inside the soluble fraction identified by GC-MS.

Figure S1: IR spectra of the OH region of the protonic HZ-15 zeolite after calcination and after inert isothermal pre-treatment

Figure S2: SEM images of (a) 17.2-MoHZ-15 and $(17.2\text{-MoHZ-15})_{N2\text{-}700°C.}$

Figure S3: Raman spectra of the catalysts 0.9-MoHZ-15 and 2.7-MoHZ-15 before and after the inert pre-treatment.

Figure S4: TEM pictures of $(17.2\text{-MoHZ-15})_{20h.}$.

Figure S5: Ion abundance of benzene as a function of the time on stream for the catalyst 2.7-MoHZ-15. The vertical drop lines correspond to the time when the reaction was stopped.

Figure S6: Thermogravimetric analysis (a) with associated CO_2-TPO profile (b) of the spent sample $(2.7\text{-MoHZ-15})_{20h}$, decomposed into two peaks: “soft” coke in blue and “hard” coke in red.

Figure S7: Example of chromatograms of the soluble coke obtained by GC-MS after the coke extraction for (a) $(0.9\text{-MoHZ-15})_{10h}$ and (b) $(0.9\text{-MoHZ-15})_{20h}$.

Figure S8: XRD patterns of the insoluble coke recovered at different time-on-stream for (a) 0.9-MoHZ-15 and (b) 2.7-MoHZ-15.

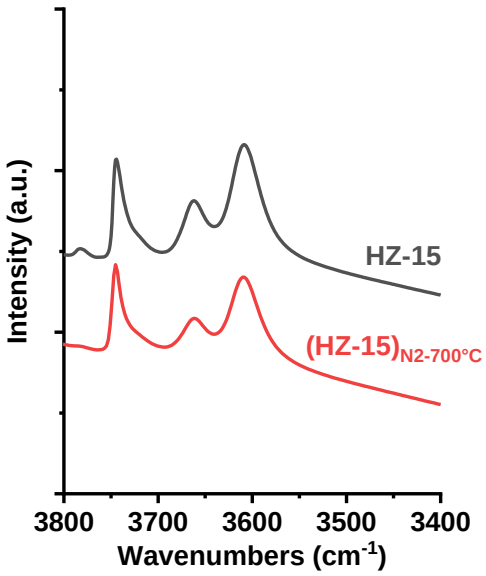

Figure S1: IR spectra of the OH region of HZ-15 zeolite after calcination and inert isothermal pre-

treatment.

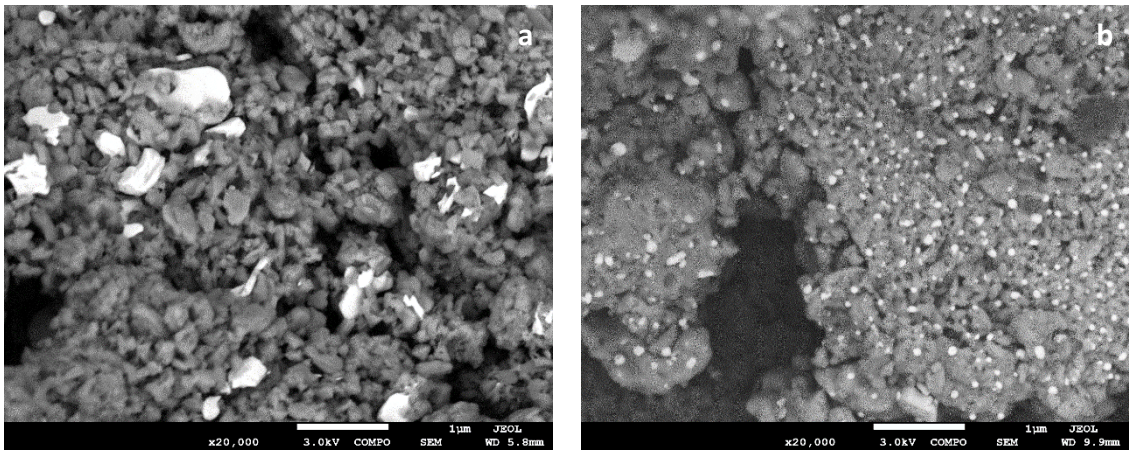

Figure S2: SEM pictures of (a) 17.2-MoHZ-15 and (17.2-MoHZ-15)$_{N2\text{-}700°C}$.

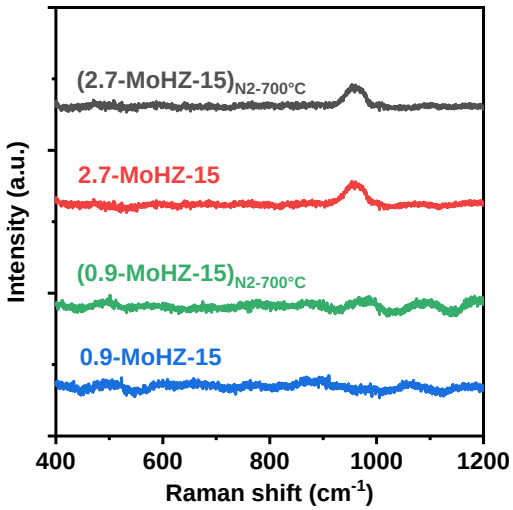

Figure S3: Raman spectra of 0.9-MoHZ-15 and 2.7-MoHZ-15 catalysts before and after inert pre-treatment.

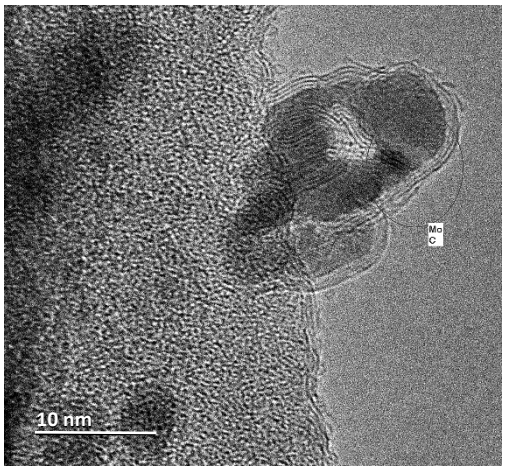

Figure S4: TEM of $(17.2\text{-MoHZ-15})_{20h}$ catalyst.

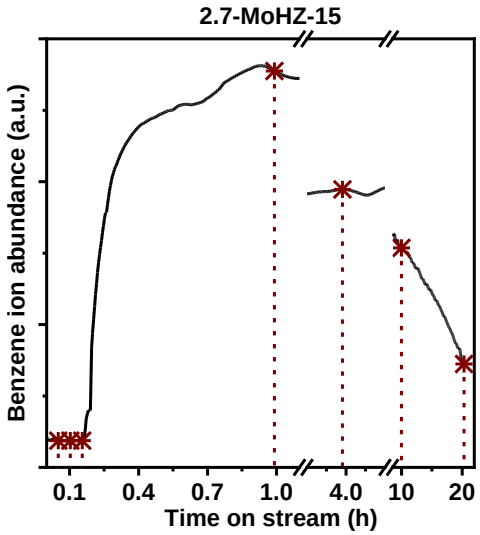

Figure S5: Ion abundance of benzene as a function of ToS for 2.7-MoHZ-15. Vertical dotted lines indicate when reaction was stopped.

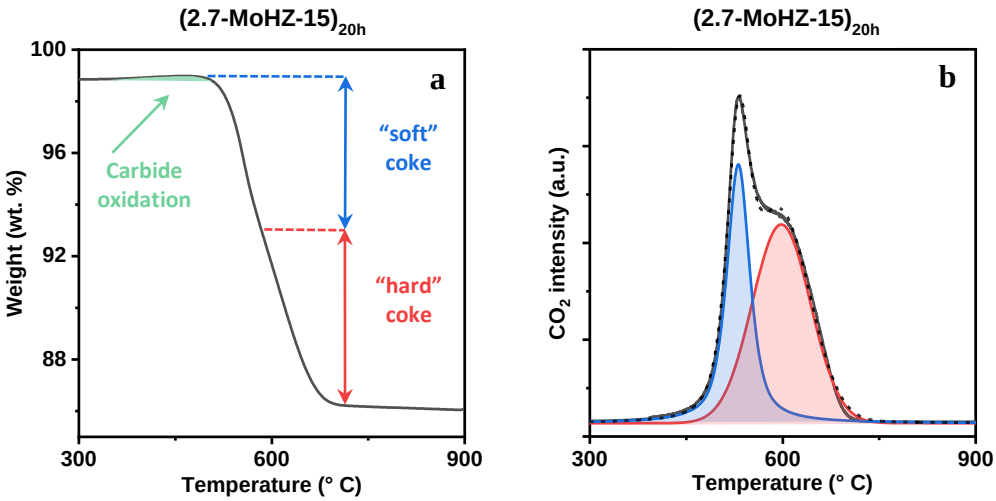

Figure S6: Thermogravimetric analysis (a) corresponding CO_2-TPO profile (b) of spent $(2.7\text{-MoHZ-15})_{20h}$ catalyst, deconvoluted into two peaks: "soft" (blue) and "hard" (red) cokes.

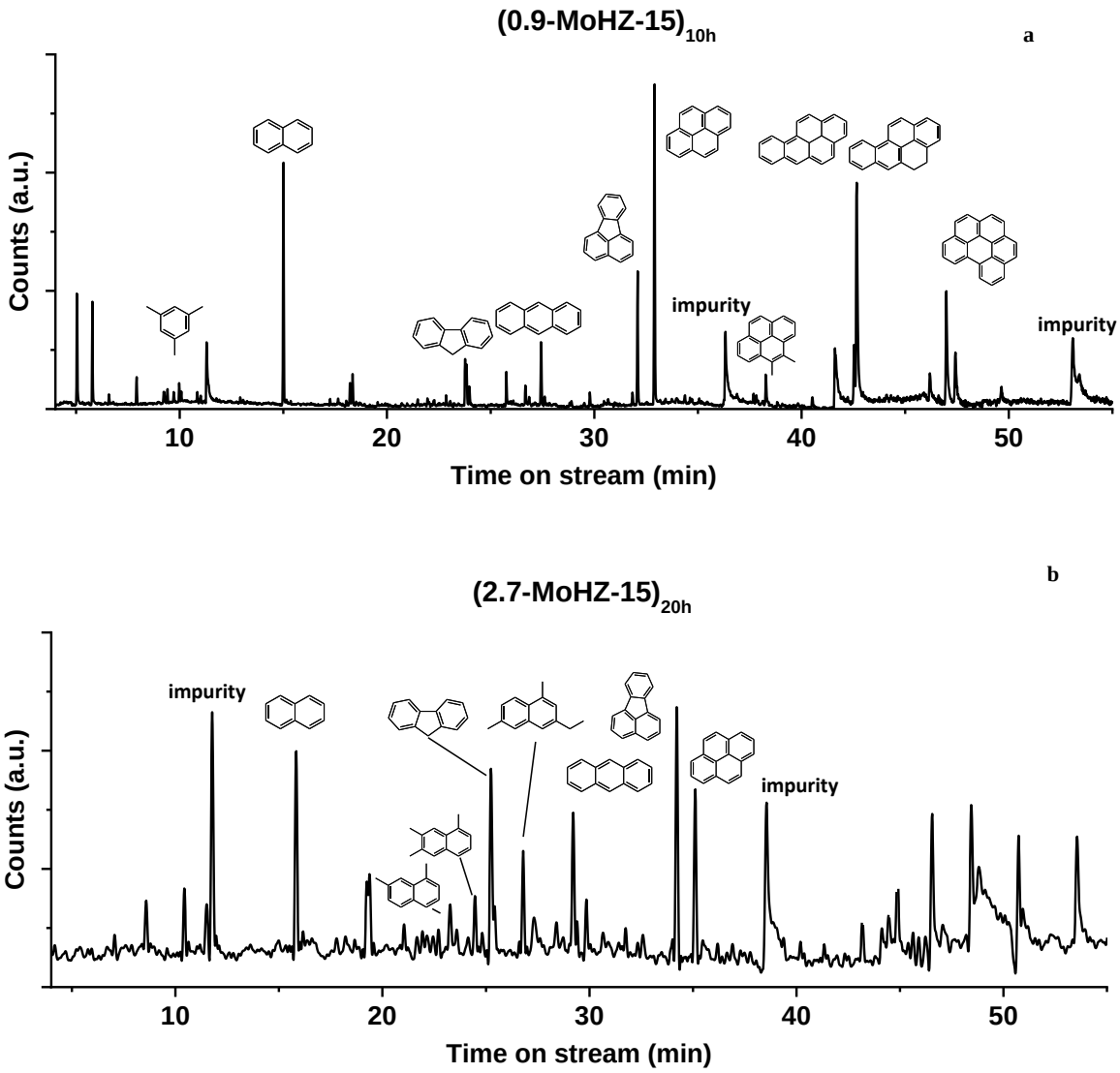

Figure S7: Chromatograms of the soluble coke obtained by GC-MS after its extraction from (a) $(0.9\text{-MoHZ-15})_{10h}$ and (b) $(2.7\text{-MoHZ-15})_{20h}$.

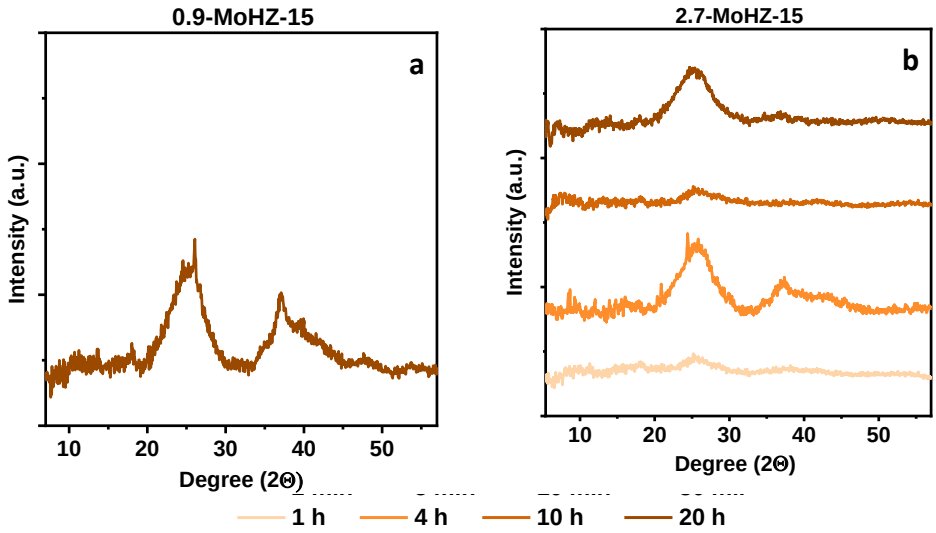

Figure S8: XRD patterns of insoluble coke recovered at different ToS for (a) 0.9-MoHZ-15 and (b) 2.7-MoHZ-15.

Table S1: Coke molecules of the soluble fraction identified by GC-MS

Nature of soluble coke				Time appearance [a]	
Unsaturation number	Name	Molecular formula (weight)	Density	Catalyst name	
				0.9-MoHZ-15	2.7-MoHZ-15
4	Toluene	C_7H_8 (92)	0.87	/	[10 min, 1 h]
	Xylenes	C_8H_{10} (106)	0.87	/	[10 min, 1 h]
	Mesitylene	C_9H_{12} (120)	0.86	[10 min, 4 h]	/
	Ethylbenzene	C_8H_{10} (106)	0.87	/	[10 min, 1 h]
7	Naphthalene	$C_{10}H_8$ (128)	1.14	[10 min, 4 h]	[10 h, 20 h]
	2,5-Dimethylnaphthalene	$C_{12}H_{14}$ (158)	/	/	[4 h, 20 h]
	1,2,5-Trimethylnaphthalene	$C_{13}H_{17}$ (173)	/	/	20 h
9	Fluorene	$C_{13}H_{10}$ (166)	1.2	[10 min, 4 h]	[1 h, 10 h]
10	Anthracene	$C_{14}H_{10}$ (178)	1.25	[10 min, 4 h]	[1 h, 20 h]
11	Cyclopenta[d,e,f] phenanthrene	$C_{15}H_{10}$ (190)	1.11	/	20 h
12	Pyrene	$C_{16}H_{10}$ (202)	1.27	[10 min, 4 h]	[1 h, 20 h]
	1,3 Dimethylpyrene	$C_{18}H_{16}$ (232)	/	[4 h, 10 h]	/
	Fluroranthene	$C_{16}H_{10}$ (202)	1.25	[10 min, 4 h]	[1 h, 10 h]
14	Cyclohexa[b]chrysene	$C_{20}H_{14}$ (254)	/	[4 h, 20 h]	/
15	Benzopyrene	$C_{20}H_{12}$ (252)	1.24	[4 h, 20 h]	/
17	Benzo[g,h,i]perylene	$C_{22}H_{22}$ (276)	1.38	[4 h, 20 h]	/

[a] Reaction time in which the coke molecule was detected on the spent catalyst. It is represented as time interval.

Table S2: Skeletal formula of the coke molecules present inside the soluble fraction identified by GC-MS.

Nature of soluble coke				Skeletal formula
Unsaturation number	Name	Molecular formula (weight)	Density	
4	Toluene	C_7H_8 (92)	0.87	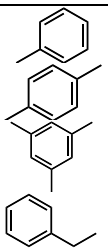
	Xylenes	C_8H_{10} (106)	0.87	
	Mesitylene	C_9H_{12} (120)	0.86	
	Ethylbenzene	C_8H_{10} (106)	0.87	
7	Naphthalene	$C_{10}H_8$ (128)	1.14	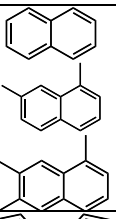
	2,5-Dimethylnaphthalene	$C_{12}H_{14}$ (158)	/	
	1,2,5-Trimethylnaphthalene	$C_{13}H_{17}$ (173)	/	
9	Fluorene	$C_{13}H_{10}$ (166)	1.2	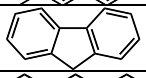
10	Anthracene	$C_{14}H_{10}$ (178)	1.25	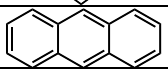
11	Cyclopenta[d,e,f] phenanthrene	$C_{15}H_{10}$ (190)	1.11	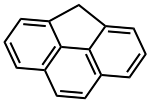
12	Pyrene	$C_{16}H_{10}$ (202)	1.27	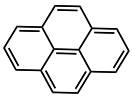
	1,3-Dimethylpyrene	$C_{18}H_{16}$ (232)	/	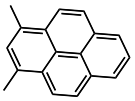
	Fluroranthene	$C_{16}H_{10}$ (202)	1.25	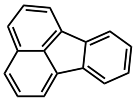
14	Cyclohexa[b]chrysene	$C_{20}H_{14}$ (254)	/	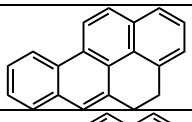
15	Benzopyrene	$C_{20}H_{12}$ (252)	1.24	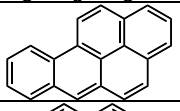
17	Benzo[g,h,i]perylene	$C_{22}H_{22}$ (276)	1.38